# Transport Efficiency of Turbulent Parcel in the Marine Boundary Layer and Its Implications for Droplet Activation in Marine Cloud Brightening

Pan Zhao[1], Jingyi Chen[1*], Yang Yang[2], Yue Jia[3] and Yang Yu[2,4]

[1]State Key Laboratory of Climate System Prediction and Risk Management, China Meteorological Administration Aerosol–Cloud and Precipitation Key Laboratory, School of Atmospheric Physics, Nanjing University of Information Science and Technology, Nanjing 210044, China
[2]State Key Laboratory of Climate System Prediction and Risk Management/Jiangsu Key Laboratory of Atmospheric Environment Monitoring and Pollution Control/Jiangsu Collaborative Innovation Center of Atmospheric Environment and Equipment Technology/Joint International Research Laboratory of Climate and Environment Change, School of Environmental Science and Engineering, Nanjing University of Information Science and Technology, Nanjing, Jiangsu, China
[3]School of Natural Sciences and Mathematics, University of Texas at Dallas, Richardson 75080, USA
[4]Department of Earth and Environmental Sciences, Faculty of Science, The Chinese University of Hong Kong, Sha Tin, Hong Kong SAR 999077, China

[*]*Correspondence to*: Jingyi Chen (jingyi.chen@nuist.edu.cn)

**Abstract.** Marine cloud brightening (MCB) aims to enhance cloud albedo by injecting sea-salt aerosols into the marine boundary layer to increase cloud droplet number concentration (CDNC). However, whether turbulent motions can efficiently transport sea-surface-released aerosols to the cloud base remains an uncertainty in evaluating MCB feasibility. This study investigates a stratocumulus case over the tropical Southeast Atlantic using large-eddy simulation (LES) coupled with the FLEXPART Lagrangian particle dispersion model to quantify turbulent parcel transport efficiency. Short-duration releases and stages of rapid liquid water path (LWP) growth favor stronger transport of turbulent parcels to the cloud base. For parcels released at 00:00 UTC on 24 September ($t_r$ = 10 min), the peak instantaneous arrival rate decreases from 3.60 % in the 900 m grid-spacing domain (d02) to 2.04 % in the 100 m grid-spacing domain (d04), while the cumulative arrival rate over the 90 min window (cropped to d04) decreases from 96.02 % to 83.35 %. The mean in-cloud residence time decreases with increasing resolution. For the subset of parcels that reach the cloud-base activation layer and exhibit positive vertical velocity within this layer, the conditional activation fraction (AF) increases with horizontal resolution, with maximum values ranging from 0.76 – 0.91 in d02 to 0.93 – 0.96 in d04. The conditional AF is insensitive to release duration but increases under high-LWP conditions. These results provide a process-level quantification of parcel transport, in-cloud residence time, and conditional activation, establishing a basis for evaluating aerosol delivery constraints in MCB applications.



删除[Pan Zhao]: -
设置格式[Pan Zhao]: 字体: 加粗, 英语(美国)
设置格式[Pan Zhao]: 英语(美国)
删除[Pan Zhao]: has been proposed as a potential climate
设置格式[Pan Zhao]: 英语(美国)
设置格式[Pan Zhao]: 英语(美国)
删除[Pan Zhao]: are introduced
设置格式[Pan Zhao]: 英语(美国)
删除[Pan Zhao]: enhance cloud albedo by increasing
设置格式[Pan Zhao]: 英语(美国)
删除[Pan Zhao]: concentrations
设置格式[Pan Zhao]: 英语(美国)
删除[Pan Zhao]: a major
设置格式[Pan Zhao]: 英语(美国)
删除[Pan Zhao]: high-LWP
删除[Pan Zhao]: ,
删除[Pan Zhao]: reaches
删除[Pan Zhao]: 39% within 15 min
删除[Pan Zhao]: , whereas it decreases
删除[Pan Zhao]: 1.86% and the peak arrival time is delay
删除[Pan Zhao]: d04;
删除[Pan Zhao]: corresponding
删除[Pan Zhao]: 94.16
删除[Pan Zhao]: 79.70%. Although the
删除[Pan Zhao]: ,
删除[Pan Zhao]: with extremely long residence times bec
删除[Pan Zhao]: parameterization, higher-resolution LES
删除[Pan Zhao]: because they better resolve strong cloud

## 1 Introduction

Marine cloud brightening (MCB) has been proposed as a potential approach to offset a portion of anthropogenic warming by introducing sea-salt aerosols into the marine boundary layer, increasing cloud droplet number concentration (CDNC) in marine low clouds, and thereby enhancing cloud albedo (Latham, 1990; Bower et al., 2006; Latham et al., 2012; Ahlm et al., 2017; Hoffmann and Feingold, 2021; Wood, 2021). Despite growing interest, MCB remains at an early stage of development and is associated with substantial scientific uncertainties regarding both its technical feasibility and its climatic effectiveness (Diamond et al., 2022; Feingold et al., 2024; Rasch et al., 2024). Among these uncertainties, the turbulent transport of sea-surface-released aerosols to the cloud base, their residence within clouds, and their subsequent activation into droplets are especially important for evaluating whether seeding can produce an observable brightening signal (Diamond et al., 2020; Dhandapani et al., 2025).

Recent large-eddy simulation (LES) studies have shown that aerosol plumes can be transported preferentially to the cloud base by coherent updrafts, suggesting that unresolved or poorly represented transport pathways may bias estimates of brightening efficacy (Glassmeier et al., 2021; Dhandapani et al., 2025). Although previous studies have largely relied on Eulerian diagnostics of plume evolution and cloud responses (Wang et al., 2011; Jenkins and Forster, 2013; Jenkins et al., 2013; Maalick et al., 2014; Chun et al., 2023), Lagrangian approaches can track trajectories by following near-surface-to-cloud-base transport pathways and linking them to cloud evolution and aerosol–cloud interactions (Erfani et al., 2025). As a result, the dynamical pathways linking surface release to cloud-base arrival and subsequent activation remain insufficiently quantified from a Lagrangian perspective.

In-cloud residence time is particularly relevant to aerosol activation because activation depends not only on whether parcels reach the cloud base, but also on whether they experience sufficiently strong and sustained supersaturation. Brief exposure to supersaturated conditions may leave a substantial fraction of parcels interstitial rather than activated, thereby reducing the effective activation fraction (AF) and weakening the cloud response (Nenes et al., 2001; VanReken et al., 2003; Peng et al., 2005; Grabowski and Wang, 2013; Chen et al., 2018). This issue is especially important for MCB, where the climatic impact depends on the efficiency of the full transport–activation chain rather than on aerosol injection alone.

A related uncertainty concerns the turbulent upward transport of parcels released near the sea surface. In practical seeding scenarios, parcels must first overcome local stabilization associated with evaporative cooling and then be lofted by boundary-layer turbulence to the cloud base (Russell et al., 1999; Wang et al., 2011; Jenkins and Forster, 2013; Prabhakaran et al., 2023; Hernandez-Jaramillo et al., 2023). Even after reaching the cloud base, activation remains sensitive to local supersaturation, updraft strength, aerosol size distribution, and residence time (Abdul-Razzak and Ghan, 2000; Fountoukis and Nenes, 2005; Xue et al., 2008; Morales Betancourt and Nenes, 2014; Hoffmann et al., 2022). These coupled dynamical

删除[Pan Zhao]: concentrations

删除[Pan Zhao]: However, most existing analyses rely primarily

设置格式[Pan Zhao]: 英语(英国)

删除[Pan Zhao]: or grid-mean

删除[Pan Zhao]: , offering only limited insight on individual parcel histories, such as transport timing,

删除[Pan Zhao]: entry, and in-cloud residence time. Since these diagnostics cannot directly resolve parcel pathways from the

删除[Pan Zhao]: layer

删除[Pan Zhao]: the

删除[Pan Zhao]:

删除[Pan Zhao]: , a Lagrangian framework is required

删除[Pan Zhao]: link parcel transport histories with subsequent

删除[Pan Zhao]: -base activation.

设置格式[Pan Zhao]: 英语(美国)

删除[Pan Zhao]: pathway

删除[Pan Zhao]: remains

删除[Pan Zhao]: -

and microphysical controls motivate a process-oriented assessment of MCB in realistic marine stratocumulus environments (Stevens, 2002; Matheou and Teixeira, 2019).

Diamond et al. (2022) identified a key technical feasibility "off-ramp": the need to demonstrate that appropriately sized particles can be generated and transported through a real marine boundary layer, activate efficiently near the cloud base, and ultimately produce measurable optical brightening. Addressing this requirement calls for a framework that links boundary-layer transport directly to activation-relevant parcel histories. A Lagrangian analysis embedded in high-resolution meteorological simulations is therefore well suited to isolate the physical bottlenecks in the MCB pathway.

In this study, we combine LES with the FLEXPART Lagrangian particle dispersion model to examine a persistent stratocumulus case over the tropical Southeast Atlantic (SEA). Passive Lagrangian tracers released near the sea surface are used as numerical proxies for turbulent parcel transport. We quantify transport efficiency, transport timing, and in-cloud residence time under different release scenarios and model resolutions, and we further examine the potential implications of these transport pathways for conditional cloud droplet activation at the cloud base, i.e., activation diagnosed for parcels that actually reach the cloud-base activation layer (Sect. 3.4). We therefore investigate the coupled transport–activation pathway of turbulent parcels within the marine boundary layer. Specifically, we examine (1) the transport efficiency of turbulent parcels from the near-surface layer to the cloud base and (2) how the thermodynamic histories of these turbulent parcels influence particle activation potential near the cloud base. By linking parcel transport dynamics with a simplified activation analysis, this study provides a Lagrangian-based quantification of the transport–residence–activation pathway relevant to assessing aerosol delivery to the cloud base in MCB applications.

## 2 Methods

This section describes the model configurations and datasets used in this study. Case selection is based on the agreement in low-cloud fraction between ERA5 and MODIS. The selected case is then simulated using WRF version 4.6, with ERA5 providing the initial and lateral boundary conditions and a nested configuration spanning horizontal grid spacings from 2.7 km to 100 m (Sect. 2.4). Model evaluation uses MODIS cloudy liquid water path (LWP), CERES shortwave cloud radiative effect (SWCRE), and CALIPSO/CALIOP cloud base height (CBH), with ERA5 providing additional reference estimates of CBH, LWP, and SWCRE at the top of the atmosphere and the surface. Finally, FLEXPART-WRF is driven by the simulated WRF meteorological fields to diagnose turbulent parcel transport (Sect. 2.5). Further details are provided in the following subsections.

删除[Pan Zhao]: .
设置格式[Pan Zhao]: 英语(美国)
删除[Pan Zhao]: -
设置格式[Pan Zhao]: 英语(美国)
删除[Pan Zhao]: and the associated microphysical responses
设置格式[Pan Zhao]: 英语(美国)
删除[Pan Zhao]: -
删除[Pan Zhao]: -

### 2.1 Reanalysis dataset

We use the European Centre for Medium-Range Weather Forecasts (ECMWF) Reanalysis 5th Generation (ERA5) dataset (Hersbach et al., 2020). The data cover the period from 00:00 UTC on 23 September to 00:00 UTC on 26 September 2009, with a horizontal resolution of 0.25°×0.25° and a 1-hour temporal resolution. This 3 d period includes model spin-up and provides the large-scale forcing for the WRF simulations. The post-spin-up period captures the LWP evolution and diurnal variability relevant to parcel transport and cloud-base activation, and is therefore sufficient for the intended analysis. ERA5 serves as the initial and lateral boundary conditions for the WRF simulations. In addition, several ERA5 variables are used during case screening and the evaluation of the simulated cloud evolution: CBH, total column liquid water (tclw; i.e., the scene-averaged LWP), and net solar radiation under all-sky and clear-sky conditions at both the top of the atmosphere (tsr, tsrc) and the surface (ssr, ssrc). The hourly accumulated radiation fields (tsr, tsrc, ssr, ssrc) in ERA5 are converted to hourly-mean fluxes, while the high-frequency WRF outputs (15 min for d01 and 1 min for d04) are likewise averaged to 1-hour intervals, enabling temporally aligned evaluations of TOA and surface SWCRE against both ERA5 and CERES satellite observations.

### 2.2 Satellite observations

To evaluate the simulation accuracy and perform case selection, we use the MODIS Level-3 daily atmospheric product (MCD06COSP_D3, Collection 6.1) from Terra and Aqua satellites, with a horizontal resolution of 1° × 1°, covering 23 – 25 September 2009. The observed LWP spatial distributions and temporal evolution are used to evaluate the WRF simulations. Note that MODIS LWP is retrieved for cloudy pixels only and thus represents cloudy (in-cloud) LWP.

To evaluate the simulated SWCRE, we use the CERES SYN1deg-1H Edition 4.2 (Edition4B) product (Rutan et al., 2015), covering 23 – 25 September 2009. This product combines CERES instrument observations from the Terra and Aqua satellites with temporally interpolated geostationary satellite data, providing TOA and surface radiative fluxes at a horizontal resolution of 1° × 1° and a temporal resolution of 1 h. In this study, SWCRE is uniformly defined as the difference between all-sky and clear-sky net shortwave fluxes (negative values indicate a cloud cooling effect); for CERES, it is derived from the difference between all-sky and clear-sky downward and upward shortwave fluxes at both the TOA and the surface, while the corresponding variables and conversions for WRF and ERA5 are described in Sects. 2.4 and 2.1, respectively.

To evaluate the simulated CBH, we use the 5-km merged layer product (CAL_LID_L2_05kmMLay, Version 5 – 00) from the CALIOP aboard the CALIPSO satellite, covering 23 September 2009. The product reports the boundaries of cloud and aerosol layers along the orbit; here we use its single-shot profiles, which have an along-track horizontal resolution of approximately 333 m. Within the study region (14.65°S – 10.00°S, 10.00°W – 5.70°W), CALIPSO passed over the region

删除[Pan Zhao]: **Dataset**

设置格式[Pan Zhao]: 英语(美国)

设置格式[Pan Zhao]: 英语(美国)

删除[Pan Zhao]:

删除[Pan Zhao]: <math>

设置格式[Pan Zhao]: 英语(美国)

删除[Pan Zhao]: Weather Research and Forecasting (WRF) simulations. Additionally, its low cloud cover and liquid water path (LWP) time series are used as references for both case screening and evaluation of simulated cloud evolution.

删除[Pan Zhao]: Moderate Resolution Imaging Spectroradiometer (MODIS)

删除[Pan Zhao]: <math>

删除[Pan Zhao]: 23-25

删除[Pan Zhao]: MODIS low cloud cover is used to evaluate ERA5 cloud fraction and assist case selection. Observed

设置格式[Pan Zhao]: 字体: （中文）宋体, 英语(美国)

设置格式[Pan Zhao]: 正文

设置格式[Pan Zhao]: 英语(美国)

设置格式[Pan Zhao]: 英语(美国)

twice on 23 September, at 01:47:38 UTC and 14:06:05 UTC; no overpass covers the region on 24 September, so the CBH comparison is restricted to 23 September. The CBH is extracted profile by profile. For each single-shot profile, the reported layers are examined from the lowest one upward; layers classified as non-cloud (clear air or aerosol) and layers with a cloud–aerosol discrimination (CAD) score below 70 are discarded, and the first remaining cloud layer is taken as the lowest cloud layer of that profile. The CBH above ground level (AGL) is then obtained by subtracting the surface elevation from the layer-base altitude, which is referenced to mean sea level. Consistent with the model and reanalysis, only low-cloud samples with an AGL cloud base below 3 km are retained: a profile is excluded if its lowest cloud base exceeds 3 km or if it contains no qualifying cloud layer. The comparison with the model is constructed under two spatial configurations: over the d01 region, the profile cloud bases are averaged onto the $0.25^{\circ}$ grid, whereas over the d04 region, the original single-shot footprints are retained; the detailed spatial and temporal collocation is described in Sect. 3 and in the caption of Fig. 2.

### 2.3 Case selection

We focus on the tropical SEA region in the Southern Hemisphere (approximately 15°S – 10°S, 5°W – 10°W). This region is one of the designated areas for MCB studies, as it hosts one of the world's major persistent and expansive stratocumulus decks (Wood, 2012; Feingold et al., 2024). The SEA is of particular interest for such research due to its relatively stable large-scale meteorological forcing and the high susceptibility of cloud albedo to aerosol perturbations (Zelinka et al., 2017; Diamond et al., 2020). It therefore represents a suitable region for investigating turbulent transport efficiency within the marine boundary layer and the mechanisms of cloud-droplet activation. We select a case where the low cloud fraction from the ERA5 reanalysis closely matches MODIS observations, thereby increasing confidence in the meteorological forcing field. Specifically, during the simulation period from 23 to 25 September, the ERA5 low cloud fractions are 56.90 %, 57.52 %, and 52.43 %, respectively, which exhibit good agreement with the MODIS observations of 57.28 %, 57.32 %, and 56.72 %. The consistency between ERA5 and MODIS low cloud fractions on 23 and 24 September justifies the selection of this period for analysis of parcel transport with a realistically represented stratocumulus cloud environment. Consequently, while the entire three-day period is simulated, our subsequent analysis primarily focuses on 23 and 24 September to leverage the most accurate meteorological forcing for the Lagrangian trajectory study.

### 2.4 WRF simulation

We use WRF version 4.6, operated in LES mode in the inner nested domains, with a four-domain one-way nested grid configuration (Skamarock et al., 2019). The horizontal grid spacings and domain extents are 2.7 km for d01 (15.04°S – 9.94°S, 10.11°W – 4.89°W), 900 m for d02 (12.73°S – 10.99°S, 9.14°W – 7.32°W), 300 m for d03 (12.33°S – 11.51°S, 8.65°W – 7.82°W), and 100 m for d04 (12.17°S – 11.72°S, 8.46°W – 8.00°W) (Fig. 1). Of the inner domains, only the 100 m grid spacing of d04 falls within the range typically used for boundary-layer LES, whereas the 900



设置格式[Pan Zhao]: 英语(美国)
删除[Pan Zhao]: <math>
删除[Pan Zhao]: <math>
设置格式[Pan Zhao]: 英语(英国)
设置格式[Pan Zhao]: 英语(英国)
删除[Pan Zhao]: datasets
设置格式[Pan Zhao]: 英语(英国)
设置格式[Pan Zhao]: 英语(英国)
删除[Pan Zhao]: fraction during
设置格式[Pan Zhao]: 英语(英国)
设置格式[Pan Zhao]: 英语(英国)
删除[Pan Zhao]: layer
删除[Pan Zhao]: <math>
删除[Pan Zhao]: <math>
删除[Pan Zhao]: <math>
删除[Pan Zhao]: <math>
删除[Pan Zhao]: <math>
删除[Pan Zhao]: <math>
删除[Pan Zhao]: <math>

m (d02) and 300 m (d03) grids span the transition toward this regime; the nested d02 – d04 design is therefore used to quantify the sensitivity of the diagnosed parcel transport and cloud-base activation to grid spacing (Sects. 3.3 – 3.4). The simulations are initialized with ERA5 reanalysis data and are driven at the lateral boundaries by ERA5 throughout the simulation period. Cloud microphysical processes are represented by the Thompson microphysics scheme (Thompson et al., 2008). Shortwave and longwave radiation are parameterized using the Rapid Radiative Transfer Model for GCMs (RRTMG; Iacono et al., 2008). Surface and near-surface processes are represented by the Monin-Obukhov (Janjic Eta) surface layer scheme and the Unified Noah land surface model (Janjić, 1994; Tewari et al., 2004). The Mellor-Yamada-Janjić (MYJ) planetary boundary layer (PBL) scheme is applied only in the outermost domain (d01) to represent sub-grid mixing. In contrast, the PBL scheme is turned off in the inner nested domains (d02, d03, and d04), where the model explicitly resolves the major turbulent motions (Janjić, 1994). To capture rapidly evolving turbulent structures and support accurate Lagrangian tracking, the model history output interval is set to 1 min for d02–d04 and to 15 min for d01. This temporal resolution allows us to better document the buoyancy-driven pathways of turbulent parcels and their residence times near cloud base. The main WRF configurations used in this study are summarized in Table 1. The WRF diagnostics used for the evaluation include the cloud water mixing ratio (QCLOUD), the downward and upward shortwave fluxes at TOA (SWDNT and SWUPT) together with their clear-sky counterparts (SWDNTC and SWUPTC), and the corresponding surface fluxes (SWDNB, SWUPB, SWDNBC, and SWUPBC). The WRF LWP is calculated only for cloud columns with QCLOUD $\geq 10^{-6}$ kg kg$^{-1}$ at any model level and therefore also represents cloudy (in-cloud) LWP, consistent with the MODIS definition (Sect. 2.2). SWCRE at both the TOA and the surface is derived from these fluxes and their clear-sky counterparts. The WRF CBH is defined as the height above ground of the lowest model level with QCLOUD $\geq 10^{-6}$ kg kg$^{-1}$, and, consistent with CALIPSO (Sect. 2.2) and ERA5 (Sect. 2.1), only columns with a cloud base below 3 km are retained; the identical diagnostic is applied to d01 and d04 (Fig. 2d).

### 2.5 FLEXPART-WRF turbulent parcel transport simulations

We use FLEXPART-WRF (i.e., FLEXPART configured to use WRF output as input, version 3.2; Brioude et al., 2013) to simulate Lagrangian transport of turbulent parcels within the marine boundary layer, driven by three-dimensional WRF meteorological fields (Table 1). The fields passed from WRF to FLEXPART include winds, pressure, geopotential, temperature, water vapor, and near-surface meteorological variables. Turbulent dispersion is represented using the Hanna et al. (1982) parameterization, which diagnoses turbulent velocity fluctuations and Lagrangian time scales rather than directly using WRF turbulent kinetic energy (TKE). Although this scheme may not be optimal at LES resolutions (Cornwell et al., 2021), it is applied consistently across domains to provide a common baseline for assessing differences in transport efficiency associated with the resolved air motion. Boundary-layer height is diagnosed internally using a critical Richardson number method (Vogelezang and Holtslag, 1996).

删除[Pan Zhao]: mp_physics = 8;

删除[Pan Zhao]: ra_sw_physics = 4, ra_lw_physics = 4;

删除[Pan Zhao]: (sf_sfclay_physics = 2)

删除[Pan Zhao]: sf_surface_physics = 2;

删除[Pan Zhao]: bl_pbl_physics = 2 for

删除[Pan Zhao]: bl_pbl_physics = 0 for

删除[Pan Zhao]: operates at LES scales and

删除[Pan Zhao]: -

删除[Pan Zhao]: (history_interval = 1, 1, 1)

删除[Pan Zhao]: (history_interval = 15).

设置格式[Pan Zhao]: 英语(美国)

删除[Pan Zhao]: , based on the model framework describ…

删除[Pan Zhao]: . (

删除[Pan Zhao]: ),

删除[Pan Zhao]: evaluate the

删除[Pan Zhao]: characteristics

删除[Pan Zhao]: . FLEXPART-WRF is

删除[Pan Zhao]: from WRF

删除[Pan Zhao]: operates within a Lagrangian framework…

删除[Pan Zhao]: mixing, random-walk diffusion, and vertical

删除[Pan Zhao]: processes (Stohl et al., 2005; Jia et al., 2…

删除[Pan Zhao]: using the FLEXPART-ECMWF …

Our method is different from McMichael et al. (2024, 2026), who used an independent Langevin particle model driven by LES-derived turbulence statistics, such as velocity variances and turbulent dissipation rates, to investigate horizontal dispersion. FLEXPART-WRF is run offline using archived WRF meteorological fields, with passive Lagrangian tracers released near the sea surface to represent turbulent air parcels rather than individual aerosol particles. Air parcels are released from five spatially distinct source regions (Boxes 1 – 5) located in the southeastern corner of the domain (Fig. 1d) to ensure spatial representativeness under the prevailing southeasterly winds over the SEA. Each box measures 5 km × 5 km, with 2 km spacing between adjacent boxes. A total of 50 000 parcels (10 000 per box) are released from five regions at 0 – 20 m above the sea surface to represent turbulent air transport near MCB sprayers. This configuration is consistent with previous FLEXPART-WRF and LES studies using near-surface releases (Cornwell et al., 2021; Salter et al., 2008; Kainz et al., 2026). The parcels are passive tracers without prescribed aerosol sizes or emission rates, which are considered separately in the activation analysis (Sect. 3.4). Thus, parcel counts represent numerical sampling rather than physical aerosol concentrations, and the diagnosed transport efficiency excludes aerosol-specific processes such as inertia, settling, deposition, and aerosol–meteorology interactions. Two release settings are considered (Table 2).

We conducted the sensitivity studies following the aspects below (30 experiments in total):

(1) Release duration

Two release durations are considered: 10 min and 60 min. The 10 min experiment represents a pulse release, whereas the 60 min experiment represents a sustained release.

(2) Release timing

Releases are initiated at different phases of LWP evolution during the simulation period, including 14:00 UTC on 23 September 2009 (LWP minimum), 22:00 UTC on 23 September 2009, 00:00 UTC on 24 September 2009, 02:00 UTC on 24 September 2009 (LWP maximum), and 06:00 UTC on 24 September 2009 (Fig. 2a). These release times sample different stages of cloud development to assess transport variability under evolving meteorological conditions. Each release time-duration combination is simulated independently using offline FLEXPART-WRF, with passive tracers that do not affect WRF meteorology or cloud properties. Cloud droplet activation is diagnosed separately in post-processing (Sect. 3.4), ensuring no carry-over effects between experiments.

For the transport analysis, cloud base is identified as the first model level at which the cloud water mixing ratio exceeds $10^{-6}$ kg $kg^{-1}$, consistent with the cloud-column threshold used for the LWP calculation in Sect. 2.4 and with cloud-mask thresholds commonly used in previous WRF studies (Arbizu-Barrena et al., 2015). Parcel transport is evaluated based on the first arrival of parcels at cloud base. The temporal evolution of parcel transport is characterized by the instantaneous arrival rate, defined as the fraction of released parcels first arriving at cloud base at each time step, with the total number of released parcels fixed at 50 000 for each experiment. The cumulative arrival rate is then obtained by integrating the instantaneous



设置格式[Pan Zhao]: 英语(英国)
删除[Pan Zhao]: and Lagrangian time scales from WRF
设置格式[Pan Zhao]: 英语(英国)
删除[Pan Zhao]: winds (WIND_OPTION = -1) to reduce
设置格式[Pan Zhao]: 英语(美国)
删除[Pan Zhao]: ,
设置格式[Pan Zhao]: 英语(美国)
删除[Pan Zhao]: are used as numerical proxies for
设置格式[Pan Zhao]: 英语(美国)
设置格式[Pan Zhao]: 英语(美国)
删除[Pan Zhao]: . Parcels
设置格式[Pan Zhao]: 英语(美国)
删除[Pan Zhao]: 1-5
设置格式[Pan Zhao]: 英语(美国)
设置格式[Pan Zhao]: 英语(美国)
设置格式[Pan Zhao]: 英语(美国)
删除[Pan Zhao]: <math> horizontal and vertical
设置格式[Pan Zhao]: 英语(美国)
删除[Pan Zhao]: are released
设置格式[Pan Zhao]: 英语(美国)
删除[Pan Zhao]: within 0-20 m
设置格式[Pan Zhao]: 英语(美国)
删除[Pan Zhao]: , consistent with typical MCB injection
设置格式[Pan Zhao]: 英语(美国)
删除[Pan Zhao]: :
设置格式[Pan Zhao]: 英语(美国)
删除[Pan Zhao]:
删除[Pan Zhao]: 2

arrival rate over time and represents the fraction of released parcels that reach cloud base over the full analysis period. In this study, transport efficiency specifically refers to the cumulative arrival rate.

To further assess the sensitivity of parcel transport to model grid spacing, parcel releases are also conducted in domains d02 – d04. To assess the implications of parcel transport for droplet formation after parcels reach cloud base, we apply a simplified single-mode activation analysis to parcels arriving at cloud base. This analysis is intended to provide activation-relevant context rather than to simulate aerosol spraying directly.

删除[Pan Zhao]:

删除[Pan Zhao]: <math>

**Table 1. Main WRF and FLEXPART-WRF configurations used in this study.**

| Model | Option | Setting | Description |
|---|---|---|---|
| WRF | mp_physics | 8 | Thompson microphysics scheme |
| | ra_sw_physics | 4 | RRTMG shortwave radiation scheme |
| | ra_lw_physics | 4 | RRTMG longwave radiation scheme |
| | sf_sfclay_physics | 2 | Monin-Obukhov (Janjic Eta) surface layer scheme |
| | sf_surface_physics | 2 | Noah land surface model |
| | bl_pbl_physics | 2 (d01), 0 (d02 – d04) | MYJ PBL scheme in d01; no PBL scheme in inner domains (d02 – d04) |
| | history_interval | 15 (d01), 1 (d02 – d04) | Output interval in minutes |
| FLEXPART-WRF | TURB_OPTION | 1 | Turbulence diagnosed as in FLEXPART-ECMWF |
| | WIND_OPTION | -1 | Vertical velocity derived from mass-consistent horizontal wind divergence |
| | SFC_OPTION | 0 | Default computation of friction velocity, surface heat flux, and PBL height |
| | CBL_SCHEME | 1 | Skewed-turbulence scheme for the convective boundary layer |
| | source regions | 5 boxes | Five release boxes in the southeastern corner of the domain |
| | parcel number | 50 000 | Total number of released parcels |
| | release height | 0 – 20 m | Near-surface release layer |

**Table 2. Overview of the 30 FLEXPART-WRF parcel-release experiments.**

| Domain | Release timing (UTC) | Release duration (min) |
|---|---|---|
| d02 | 23 14:00 | 10 |
| | 23 14:00 | 60 |
| | 23 22:00 | 10 |
| | 23 22:00 | 60 |
| | 24 00:00 | 10 |
| | 24 00:00 | 60 |
| | 24 02:00 | 10 |
| | 24 02:00 | 60 |
| | 24 06:00 | 10 |
| | 24 06:00 | 60 |
| d03 | 23 14:00 | 10 |
| | 23 14:00 | 60 |
| | 23 22:00 | 10 |
| | 23 22:00 | 60 |
| | 24 00:00 | 10 |
| | 24 00:00 | 60 |
| | 24 02:00 | 10 |
| | 24 02:00 | 60 |
| | 24 06:00 | 10 |
| | 24 06:00 | 60 |
| d04 | 23 14:00 | 10 |
| | 23 14:00 | 60 |
| | 23 22:00 | 10 |
| | 23 22:00 | 60 |
| | 24 00:00 | 10 |
| | 24 00:00 | 60 |
| | 24 02:00 | 10 |
| | 24 02:00 | 60 |
| | 24 06:00 | 10 |
| | 24 06:00 | 60 |

## 3 Results and Discussion

### 3.1 Evaluation of the Simulated Cloud and Boundary-Layer Environment

To evaluate the meteorological background for Lagrangian transport, Fig. 1 shows the cloudy LWP distribution at 02:00 UTC on 24 September 2009. The d01 region exhibits a relatively homogeneous stratocumulus field, with a mean LWP of 136.11 g $m^{-2}$ and a maximum of 346.66 g $m^{-2}$. As grid spacing decreases, finer-scale cloud structures and LWP variability become increasingly resolved, with d04 exhibiting a mean LWP of 86.65 g $m^{-2}$ and a maximum of 632.13 g $m^{-2}$. These finer-scale structures provide more detailed representations of cloud and boundary-layer variability for subsequent parcel transport analysis.

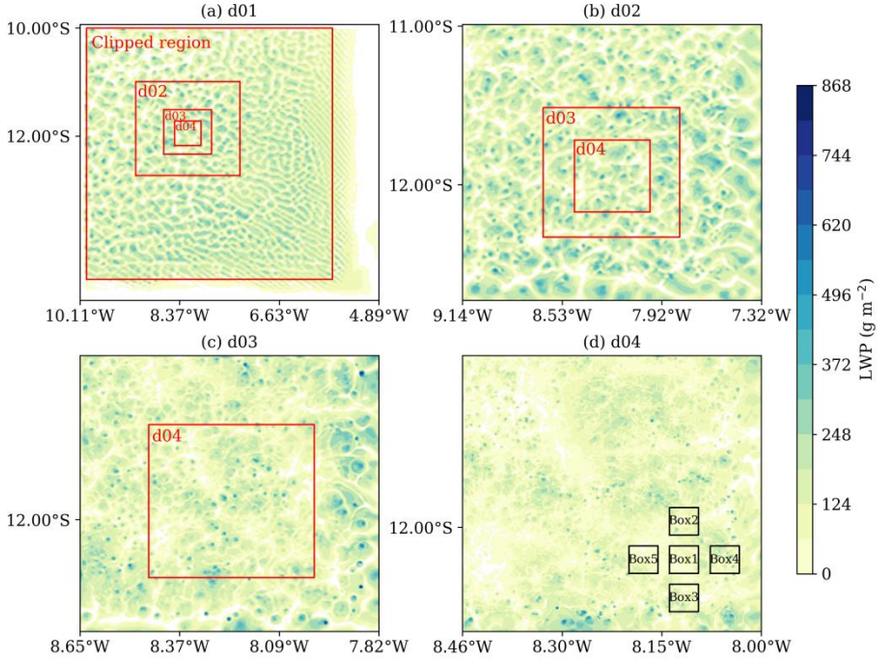



**Figure 1. Spatial distribution of instantaneous cloudy LWP (unit: g $m^{-2}$) for the nested domains d01 – d04 at 02:00 UTC on 24 September 2009: (a) d01 (mean = 136.11, max = 346.66), and the boundaries of d02 – d04; (b) d02 (mean = 135.48, max = 500.47), with red boxes indicating the boundaries of d03 – d04; (c) d03 (mean = 107.91, max = 520.19), with the red box marking the d04 boundary; and (d) d04 (mean = 86.65, max = 632.13), where black boxes denote the five sampling areas (Boxes 1 – 5). The mean and maximum LWP values for all four domains are calculated over the area covered by d04.**

To evaluate the simulated cloud field and boundary-layer structure, Fig. 2 compares WRF LWP, SWCRE, and CBH with MODIS, CERES, CALIPSO, and ERA5. WRF d01 reproduces the observed increase in LWP from 23 to 24 September indicated by MODIS, whereas ERA5 shows the opposite trend (Figs. 2a, b). Although d04 captures the same trend as



删除[Pan Zhao]: **Model Validation: Spatiotemporal**
删除[Pan Zhao]: **LWP**
设置格式[Pan Zhao]: 字体: （中文）Times New Roma
删除[Pan Zhao]: **nested WRF simulations provide a**
设置格式[Pan Zhao]: 英语(美国)
删除[Pan Zhao]: the subsequent
设置格式[Pan Zhao]: 英语(美国)
删除[Pan Zhao]: analysis
设置格式[Pan Zhao]: 英语(美国)
设置格式[Pan Zhao]: 英语(美国)
设置格式[Pan Zhao]: 英语(美国)
删除[Pan Zhao]: instantaneous
设置格式[Pan Zhao]: 英语(美国)
删除[Pan Zhao]: In the outermost domain (d01), LWP
设置格式[Pan Zhao]: 英语(美国)
删除[Pan Zhao]: marine
设置格式[Pan Zhao]: 英语(美国)
设置格式[Pan Zhao]: 英语(美国)
删除[Pan Zhao]: <math>
设置格式[Pan Zhao]: 英语(美国)
删除[Pan Zhao]: <math> within the clipped region,
设置格式[Pan Zhao]: 英语(美国)
删除[Pan Zhao]: , the LWP field becomes progressively r
设置格式[Pan Zhao]: 英语(美国)
删除[Pan Zhao]: heterogeneity more effectively. The
设置格式[Pan Zhao]: 英语(美国)



MODIS, its mean LWP is 43 – 44 % lower than that of WRF d01 sampled over the d04 region, highlighting substantial resolution sensitivity. However, the fine resolution and limited spatial coverage of the d04 domain limit direct comparisons with coarse-resolution satellite observations; model evaluation therefore focuses primarily on d01. The higher-resolution domains are primarily used to diagnose resolution-dependent turbulent parcel transport and cloud-base activation, rather than to demonstrate improved agreement with regional-mean observations. Both WRF and ERA5 slightly underestimate the magnitude of SWCRE (Fig. 2c). Both WRF and ERA5 also underestimate CBH relative to CALIPSO (Fig. 2d), with similar bias magnitudes for WRF d01 and ERA5. Overall, WRF captures the observed cloud evolution while exhibiting resolution-dependent differences in cloud properties, providing a basis for investigating turbulent transport across grid spacings.

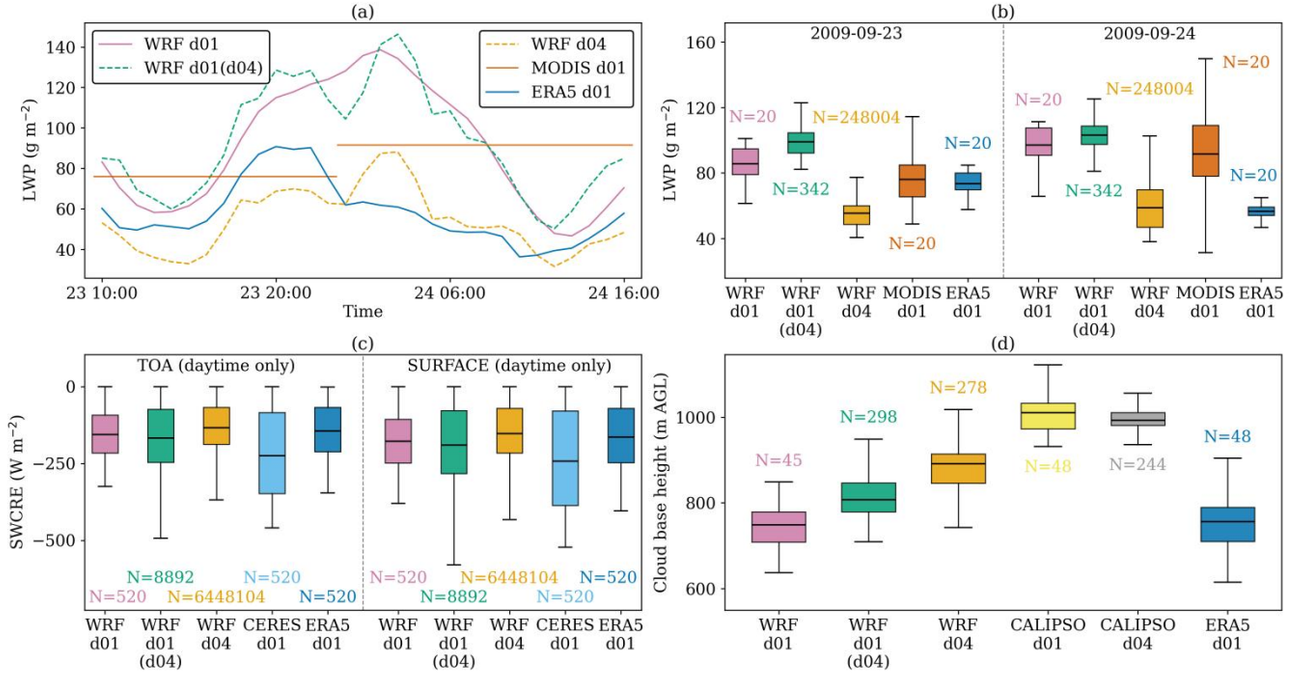



**Figure 2. Comparison of cloud and boundary-layer characteristics between WRF simulations, ERA5 reanalysis, and satellite observations. (a) Temporal evolution of LWP from 10:00 UTC on 23 September to 16:00 UTC on 24 September 2009. WRF d01, WRF d01(d04) (i.e., WRF d01 clipped to the d04 region), and WRF d04 are 1-hour averages, ERA5 provides hourly data, and MODIS provides daily means. (b) Boxplots of daily-mean LWP for 23 – 24 September. WRF d01 and ERA5 are matched to a 1° grid, WRF d01(d04) and WRF d04 retain their native grids, and MODIS is provided on its native 1° daily grid. (c) Boxplots of 1-hour mean TOA and surface SWCRE during daytime on 23 – 24 September, with data over the d01 region uniformly matched to a 1° grid, while WRF d01(d04) and WRF d04 retain their native grids. (d) Boxplots of CBH during two CALIPSO overpasses (01:47:38 and 14:06:05 UTC) on 23 September 2009; no CALIPSO data are available over the entire d01 region on 24 September. For the d01 region, CALIPSO, WRF, and ERA5 data are matched to a 0.25° grid, whereas for the d04 region, WRF d01 and WRF d04 are interpolated along the CALIPSO track to the original footprint locations. For both regions, ERA5 and WRF data are temporally matched to the CALIPSO overpass times with the corresponding spatial matching procedures. In the boxplots, boxes represent the interquartile range (IQR), and black horizontal lines indicate means; the corresponding statistics and sample size N are labeled adjacent to each box. In panel (a), WRF d01 (solid line), WRF d01(d04) (dashed line), WRF d04 (dashed line), MODIS d01 (solid line), and ERA5 d01 (solid line) are compared. Colors are kept consistent throughout the figure: WRF d01, WRF d01(d04), WRF d04, MODIS d01, ERA5 d01, CERES d01, CALIPSO d01, and CALIPSO d04 are shown in reddish purple, bluish green, orange, vermillion, blue, sky blue, yellow, and grey, respectively. All d01 data are extracted from the clipped region (14.65°S – 10.00°S, 10.00°W – 5.70°W; Fig. 1a).**

### 3.2 Meteorological Background and Thermodynamic Structure along Lagrangian Trajectories

To understand how varying meteorological conditions influence upward parcel transport across the 30 simulations, we examine the meteorological fields sampled along FLEXPART-WRF forward trajectories, focusing on the dynamical and thermodynamic processes governing marine stratocumulus-topped boundary layers (Wood, 2012; Ghate et al., 2015). The

删除[Pan Zhao]: elucidate the mechanisms driving

删除[Pan Zhao]: , this section examines

删除[Pan Zhao]: background

删除[Pan Zhao]: conditions

删除[Pan Zhao]: from FLEXPART-WRF.

vertical structures are compared across five representative stages during the evolution of LWP described in Sect. 2.5. Figure 3 presents the vertical profiles of water vapor specific humidity ($q_v$), potential temperature ($\theta$), and turbulent kinetic energy (TKE) for these release times. Since the vertical structures of these variables are broadly similar across release durations ($t_r$ = 10 min, $t_r$ = 60 min), Fig. 3 only displays the representative results for $t_r$ = 10 min with a 180 min tracking duration. All analyses in this section are based on results from domain d02.

In the supersaturated region (relative humidity, RH > 100%, Figs. 3a-c), turbulent parcels are predominantly distributed between approximately 570 and 1270 m in altitude. The vertical variations in $q_v$ and $\theta$ are generally small, with $q_v$ remaining in the range of 9.00 – 10.87 g kg$^{-1}$ and $\theta$ ranging from approximately 291.81 K to 295.72 K, indicating a high degree of thermodynamic uniformity among the different release times. In contrast, TKE varies strongly with the stages of LWP evolution, increasing from 0.08 – 0.27 m$^2$ s$^{-2}$ at 14:00 UTC on the 23rd to 0.29 – 1.27 m$^2$ s$^{-2}$ at 06:00 UTC on the 24th. This enhancement suggests that, in the early morning phase following the LWP maximum (at 02:00 UTC on the 24th), intensified longwave radiative cooling at cloud top drives vigorous vertical overturning, resulting in the strongest turbulent mixing within the cloud layer, consistent with the canonical view that nocturnal and early-morning stratocumulus turbulence is primarily maintained by cloud-top longwave radiative cooling and associated buoyancy production (Wood, 2012; Mellado, 2017).

The unsaturated layer (RH < 100%, Figs. 3d-f) spans approximately 0 – 1500 m. Within the mixed layer (0 – 1000 m), $q_v$ remains consistently high, above 8.91 g kg$^{-1}$, reflecting the abundant moisture reservoir in the marine boundary layer. Within the mixed layer, $\theta$ is stably maintained in the range of 291.57 – 292.91 K. Such a moist mixed layer capped by a sharp inversion is characteristic of subtropical marine stratocumulus environments (Wood and Bretherton, 2004; Ghate et al., 2015). Above 1000 m, during low-LWP periods (14:00 UTC on the 23rd and 06:00 UTC on the 24th), the inversion layer is lower than during other LWP phases, as indicated by $q_v$ and $\theta$. TKE peaks near the ocean surface and decreases with height, while also exhibiting a distinct peak around 1000 m. This peak is most pronounced at 00:00 and 02:00 UTC on the 24th, corresponding to the growth and mature phases of the stratocumulus layer.

To clarify how parcel thermodynamic histories differ between contrasting stages of LWP evolution, we compare two representative times: 14:00 UTC on the 23rd (LWP minimum) and 02:00 UTC on the 24th (LWP maximum). Figure 4 uses kernel density estimation (KDE) probability density functions (PDFs) to characterize the differences in parcel thermodynamic properties between the two LWP stages. In the supersaturated region (Figs. 4a-d), the PDFs at 02:00 UTC extend to higher altitudes, indicating a thicker cloud during the LWP peak phase. In the unsaturated region (Figs. 4e-h), the differences between the two LWP stages are relatively small.



删除[Pan Zhao]: 4
删除[Pan Zhao]: <math>
删除[Pan Zhao]: <math>
删除[Pan Zhao]: <math>
删除[Pan Zhao]: 4
删除[Pan Zhao]: <math>
删除[Pan Zhao]: Relative
删除[Pan Zhao]: <math>,
删除[Pan Zhao]: 4a
删除[Pan Zhao]: 510
删除[Pan Zhao]: <math>
删除[Pan Zhao]: <math>
删除[Pan Zhao]: <math>
删除[Pan Zhao]: <math>
删除[Pan Zhao]: <math>
删除[Pan Zhao]: 5
删除[Pan Zhao]: 296
删除[Pan Zhao]: <math>
删除[Pan Zhao]: <math>
删除[Pan Zhao]: .
删除[Pan Zhao]: <math>,
删除[Pan Zhao]: 4d
删除[Pan Zhao]: 0-1500 m
删除[Pan Zhao]: 0-1000 m), <math>
删除[Pan Zhao]: <math>
删除[Pan Zhao]: <math>
删除[Pan Zhao]: 291-293 K.
删除[Pan Zhao]: <math>

To identify the dynamical factor responsible for the release-time dependence of parcel transport, we further examine the vertical distribution of TKE at three key LWP stages. Figure 5 presents the KDEs of TKE at three representative phases: 14:00 UTC on the 23rd (LWP minimum), 02:00 UTC on the 24th (LWP maximum), and 06:00 UTC on the 24th, to highlight how turbulence differs between low- and high-LWP stages. In the supersaturated region (Figs. 5a-c), the maximum TKE increases much more strongly than the mean TKE across the different stages, particularly near the cloud top. This reflects enhanced cloud-top turbulent mixing during high-LWP conditions. In the unsaturated region (Figs. 5d-f), the TKE distribution displays a bimodal structure, with one peak below the cloud base ( < 200 m ) and another near the cloud top (1000 – 1250 m). The maximum TKE aloft is substantially higher at 02:00 and 06:00 UTC than at 14:00 UTC, indicating a strong sensitivity of the turbulence experienced to release timing.

These results indicate that release timing modulates parcel transport by altering both the height and depth of the saturated layer and the turbulence intensity experienced along parcel trajectories. Both factors directly influence the instantaneous and cumulative transport to the cloud base and the activation conditions encountered once turbulent parcels reach the cloud base, as discussed in the following sections.

删除[Pan Zhao]: 6

删除[Pan Zhao]: KDE distributions

删除[Pan Zhao]: key

删除[Pan Zhao]: saturated layer

删除[Pan Zhao]: 6a

删除[Pan Zhao]: 6d

删除[Pan Zhao]: (<math>

删除[Pan Zhao]: aloft above

删除[Pan Zhao]: 400-900 m

删除[Pan Zhao]: turbulence

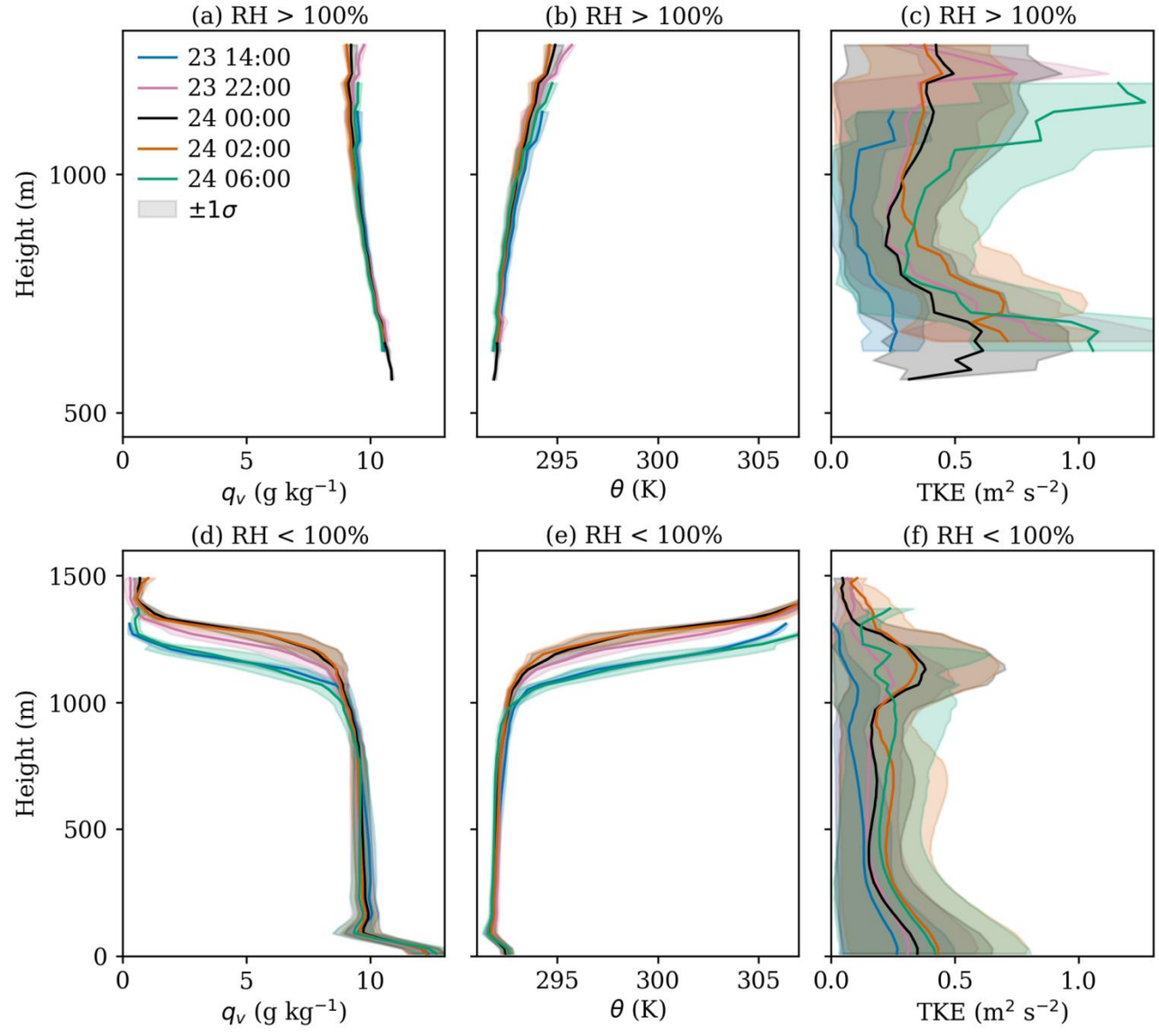
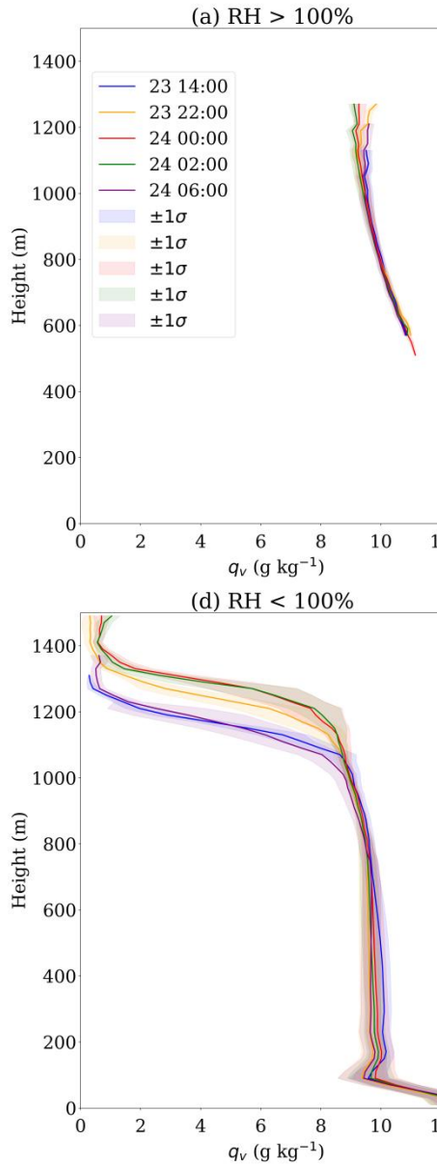



**Figure 3. Vertical profiles of background meteorological parameters for turbulent parcels at different release times ($t_r$ = 10 min, trajectory duration 180 min). (a-c) $q_v$, $\theta$, and TKE in the supersaturated region (RH > 100%). (d-f) corresponding parameters in the unsaturated region (RH < 100%). Colors indicate different times, including blue (14:00 UTC on the 23rd), reddish purple (22:00 UTC on the 23rd), black (00:00 UTC on the 24th), vermillion (02:00 UTC on the 24th), and bluish green (06:00 UTC on the 24th). Shading represents ±1σ. The unit of $q_v$ is g kg$^{-1}$. The unit of $\theta$ is K. The unit of TKE is m$^2$ s$^{-2}$.**






删除[Pan Zhao]:

删除[Pan Zhao]: **4**

删除[Pan Zhao]: <math>

删除[Pan Zhao]: <math>,<math>

删除[Pan Zhao]: <math>).

删除[Pan Zhao]: <math>).

删除[Pan Zhao]: **orange**

删除[Pan Zhao]: **red**

删除[Pan Zhao]: **green**

删除[Pan Zhao]: **purple**

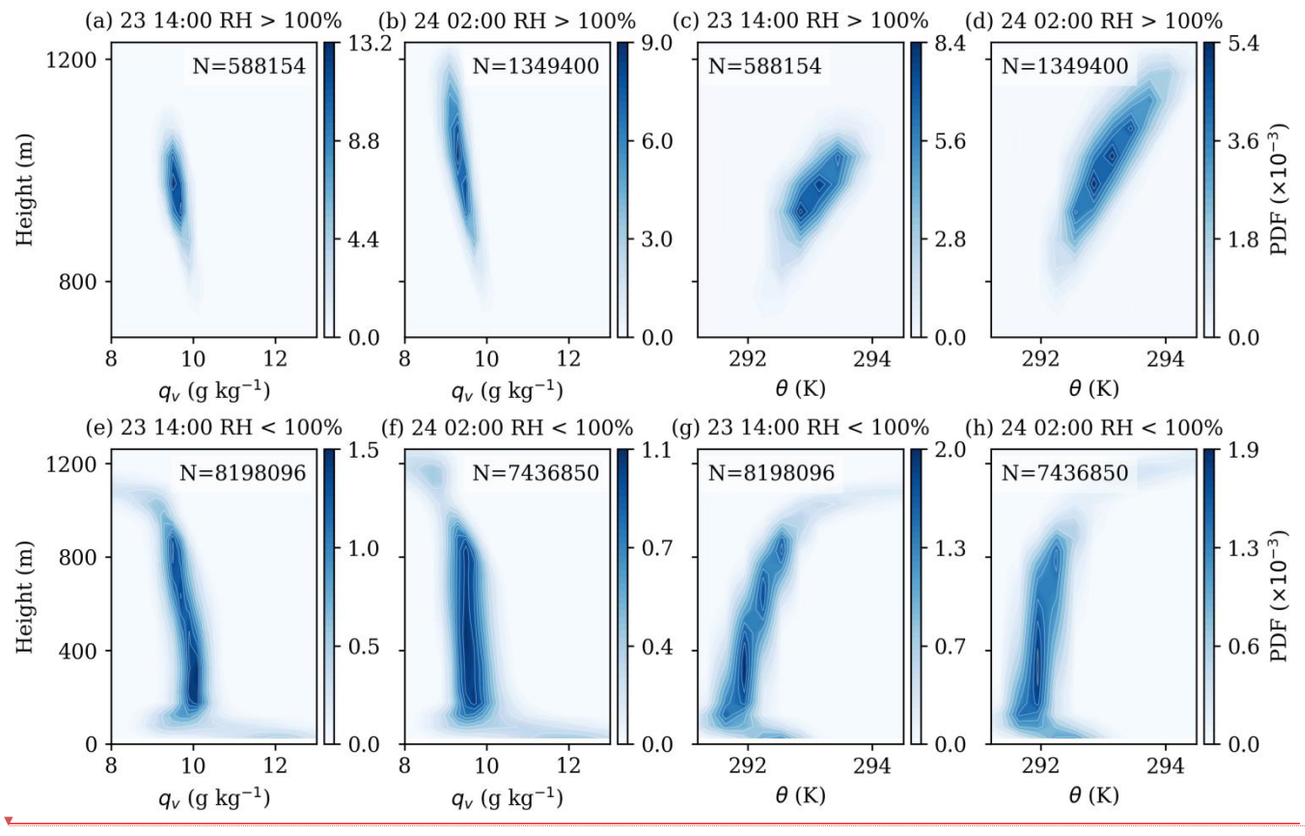
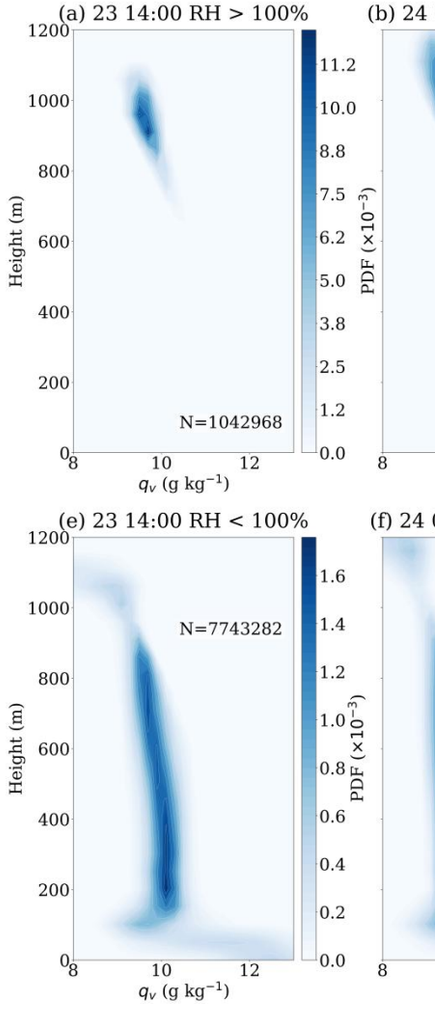



**Figure 4. KDE distributions of $q_v$ and $\theta$ as a function of height for the representative times (14:00 UTC on the 23rd and 02:00 UTC on the 24th). The upper panels show the supersaturated region (RH > 100%), and the lower panels show the unsaturated region (RH < 100%). N denotes the statistical sample size. The unit of $q_v$ is g kg$^{-1}$. The unit of $\theta$ is K.**




删除[Pan Zhao]:

删除[Pan Zhao]: **5**

删除[Pan Zhao]: <math>

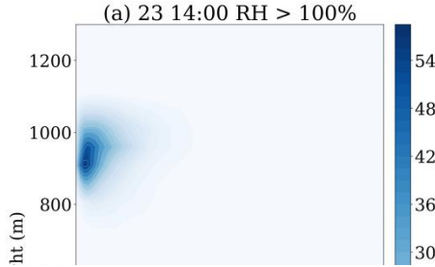
删除[Pan Zhao]: <math>

删除[Pan Zhao]: <math>**),**

删除[Pan Zhao]: <math>**).**

删除[Pan Zhao]: <math>

删除[Pan Zhao]: <math>



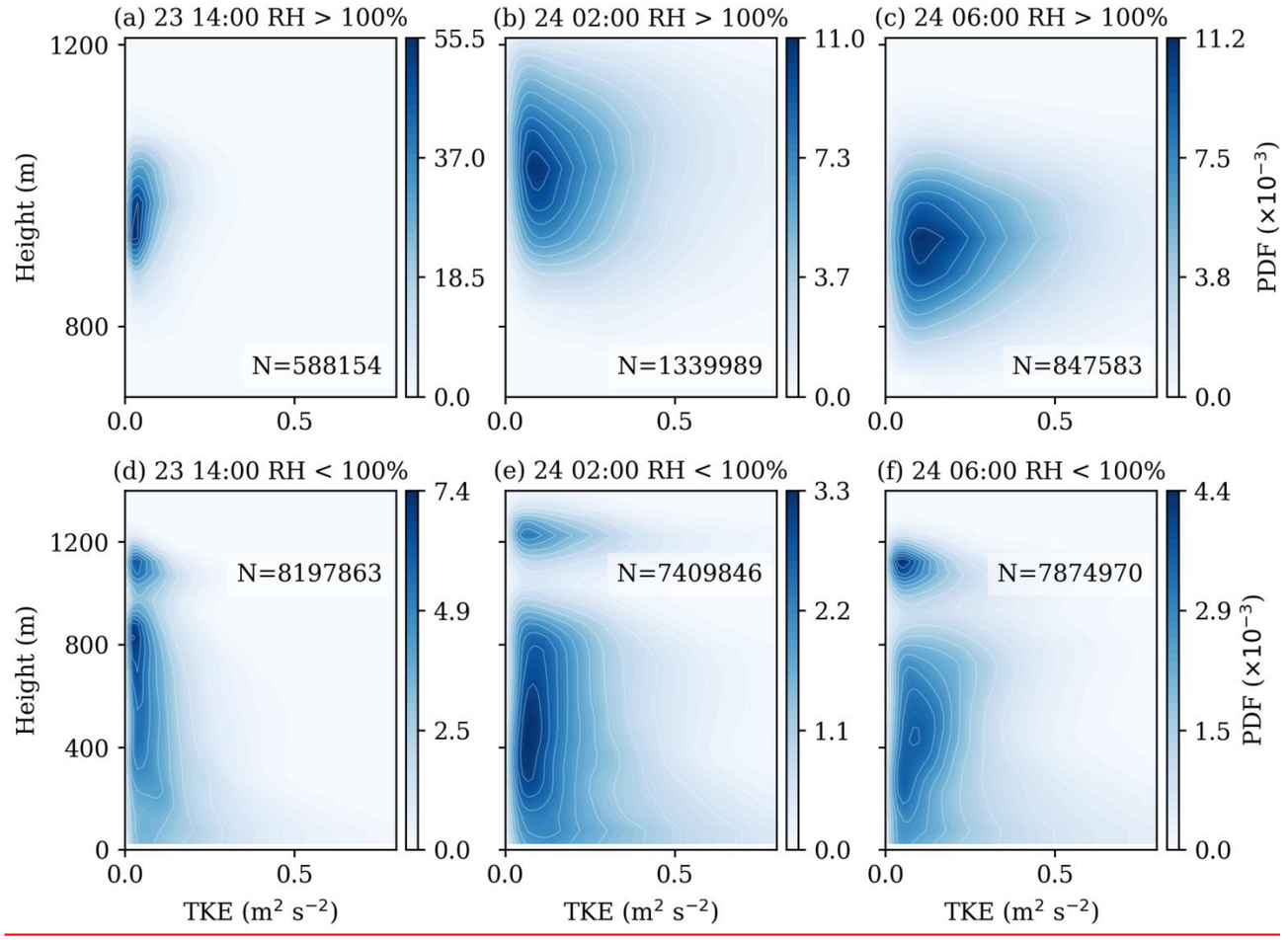



**Figure 5. PDFs of TKE as a function of height under different LWP phases (14:00 UTC on the 23rd, 02:00 UTC on the 24th, and 06:00 UTC on the 24th). The upper panels show the supersaturated region (RH > 100%), and the lower panels show the unsaturated region (RH < 100%). N denotes the statistical sample size. The unit of TKE is $m^2 s^{-2}$.**

设置格式[Pan Zhao]: 字体: 小五, 加粗, 英语(美国)

设置格式[Pan Zhao]: 正文, 行距: 单倍行距

删除[Pan Zhao]: 6

设置格式[Pan Zhao]: 字体: 小五, 加粗, 英语(美国)

设置格式[Pan Zhao]: 字体: 加粗, 英语(美国)

删除[Pan Zhao]: <math>),

设置格式[Pan Zhao]: 字体: 加粗, 英语(美国)

删除[Pan Zhao]: <math>).

设置格式[Pan Zhao]: 字体: 小五, 加粗, 英语(美国)

设置格式[Pan Zhao]: 字体: 加粗, 英语(美国)

设置格式[Pan Zhao]: 字体: 小五, 加粗, 英语(美国)

设置格式[Pan Zhao]: 字体: 加粗, 英语(美国)

删除[Pan Zhao]: <math>

设置格式[Pan Zhao]: 字体: 小五, 加粗, 英语(美国)

设置格式[Pan Zhao]: 字体: 加粗, 英语(美国)

删除[Pan Zhao]:

### 3.3 Transport Efficiency of Turbulent Parcels

This subsection evaluates how environmental factors during different LWP phases affect the transport of turbulent parcels to the cloud base. Figure 6 illustrates the temporal distribution of first arrival times at the cloud base within 180 min for five representative stages, with Fig. 6a showing the instantaneous arrival rate and Fig. 6b showing the cumulative arrival rate. With a fixed total number of parcels, the release duration ($t_r$) governs the instantaneous arrival rate. Short-duration releases ($t_r$ = 10 min, solid lines in Fig. 6a) produce burst-like peaks of 2.82 % to 3.60 % within approximately 14 min, whereas long-duration releases ($t_r$ = 60 min, dashed lines in Fig. 6a) show lower peak instantaneous arrival rates (1.50 % – 1.61 %) and delayed maxima (53 – 61 min after release). These differences indicate that shorter release intervals result in a higher temporal density of parcels entering the flow, allowing them to be transported in more concentrated groups within coherent turbulent structures. Such releases therefore capture the peak transport capacity of active updrafts more effectively, leading to the observed burst-like arrival peaks. This interpretation is consistent with previous LES studies showing that coherent updrafts can preferentially transport near-surface material toward cloud base and concentrate its delivery in space and time (Dhandapani et al., 2025). This difference primarily reflects the compressed release configuration. In contrast, the $t_r$ = 60 min cases average transport over multiple convective cycles, resulting in a broader distribution of arrival times and lower peak instantaneous arrival rates.

Figure 6b shows that, regardless of release time, more than 98 % of parcels in d02 reach the cloud base within 180 min. A shorter release duration leads to the cumulative arrival rate curves reaching a plateau earlier. Parcels released at 00:00 UTC exhibit the steepest initial increase, with the highest cumulative arrival rate, whereas those released at 14:00 UTC and in the longer-duration experiments show a slower initial increase in cumulative arrivals.

Reaching the cloud base does not guarantee droplet activation; therefore, we further examine the in-cloud residence time of parcels after cloud entry. A comparison of two contrasting phases, 14:00 UTC on the 23rd (LWP minimum) and 00:00 UTC on the 24th (the time of strongest overall transport to the cloud base), reveals distinct behaviors (Fig. 7). At 14:00 UTC (for $t_r$ = 10 min) residence times increase slowly (mean ~24 min at 120 min to ~36 min at 180 min, reaching ~51 min at 240 min), with few long-lived outliers, indicating weak mixing and limited in-cloud persistence. In contrast, at 00:00 UTC, stronger TKE and moisture supply produce a steeper increase (mean ~36 min at 120 min, ~55 min at 180 min, and ~73 min at 240 min, with third quartile (Q3) up to ~92 min and numerous high-value outliers), demonstrating that the active stratocumulus growth phase both enhances overall transport to the cloud base and substantially prolongs in-cloud residence time, thereby favoring more sustained parcel-cloud interaction. Moreover, across all groups, cumulative residence time increases with analysis period ( 60 – 240 min ), with larger means for the shorter release duration due to more concentrated cloud-base crossing, especially for the group with the strongest overall transport to the cloud base.



删除[Pan Zhao]: **efficiency**

删除[Pan Zhao]: **turbulent parcels**

删除[Pan Zhao]: 7

删除[Pan Zhao]: 7a

删除[Pan Zhao]: 7b

删除[Pan Zhao]: <math>

删除[Pan Zhao]: <math>

删除[Pan Zhao]: 7a

删除[Pan Zhao]: 45

删除[Pan Zhao]: 39

删除[Pan Zhao]: 15

删除[Pan Zhao]: <math>

删除[Pan Zhao]: 7a

删除[Pan Zhao]: 1.31%-1.58%)

删除[Pan Zhao]: 56-62 min

删除[Pan Zhao]: <math>

删除[Pan Zhao]: The instantaneous arrival rate varies wit…

删除[Pan Zhao]: 7b also

删除[Pan Zhao]: 96

删除[Pan Zhao]: approaching near-complete transport within

删除[Pan Zhao]: first 30 min

删除[Pan Zhao]: significant delays

删除[Pan Zhao]: 8

删除[Pan Zhao]: ,

删除[Pan Zhao]: median ~7

删除[Pan Zhao]: 60

删除[Pan Zhao]: 20

删除[Pan Zhao]: 29

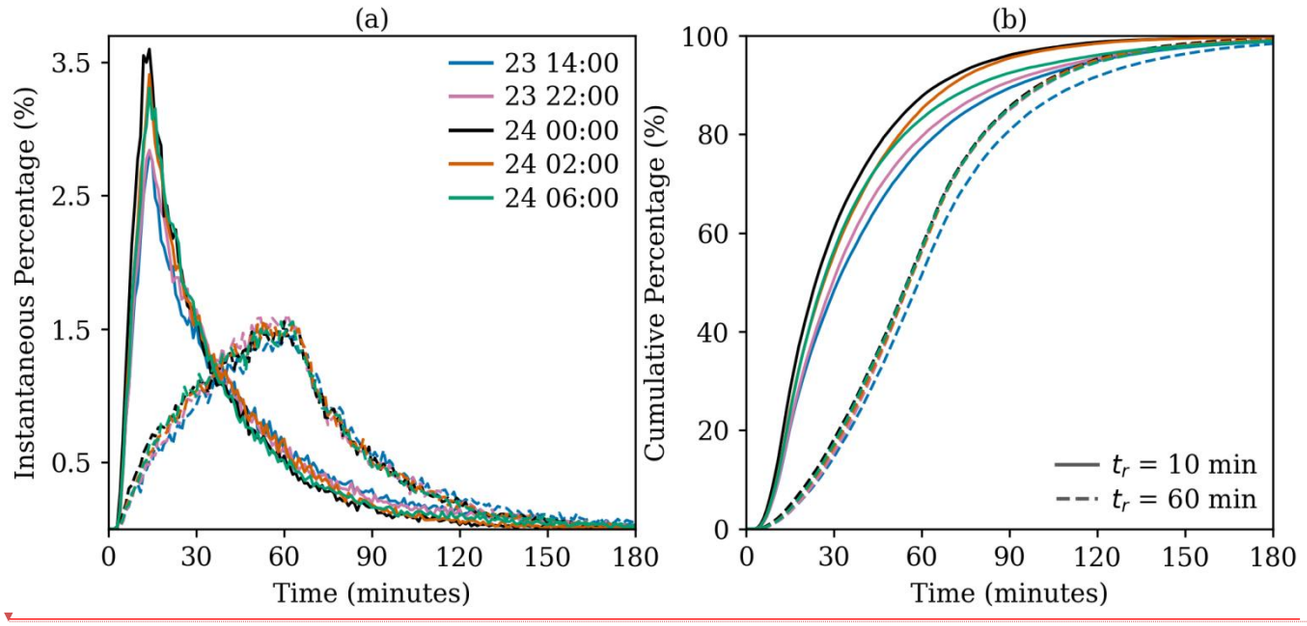



**Figure 6. Instantaneous and cumulative arrival of turbulent parcels at the cloud base for various release times. (a) Instantaneous arrival rate, defined as the percentage of total released turbulent parcels first arriving at the cloud base per minute. (b) Cumulative arrival rate, defined as the cumulative percentage of turbulent parcels arriving at the cloud base. Solid lines represent release duration $t_r$ = 10 min; dashed lines represent $t_r$ = 60 min. Colors distinguish release times: blue (14:00 UTC on the 23rd), reddish purple (22:00 UTC on the 23rd), black (00:00 UTC on the 24th), vermillion (02:00 UTC on the 24th), and bluish green (06:00 UTC on the 24th).**

删除[Pan Zhao]:

删除[Pan Zhao]: **7**

删除[Pan Zhao]: <math>

删除[Pan Zhao]: <math>.

设置格式[Pan Zhao]: 字体: 加粗, 英语(美国)

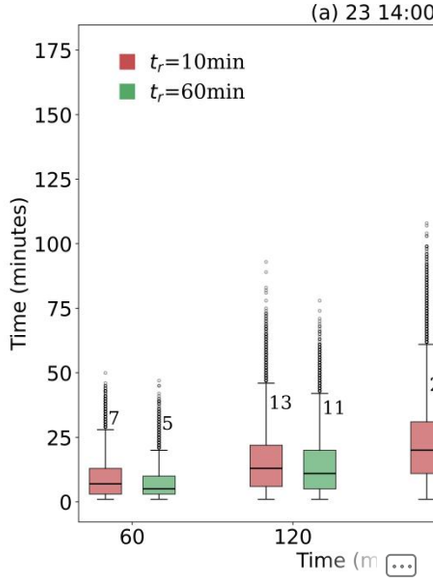
删除[Pan Zhao]: **orange**

删除[Pan Zhao]: **red**

删除[Pan Zhao]: **green**

删除[Pan Zhao]: **purple**

设置格式[Pan Zhao]: 字体: 加粗, 英语(美国)




删除[Pan Zhao]:

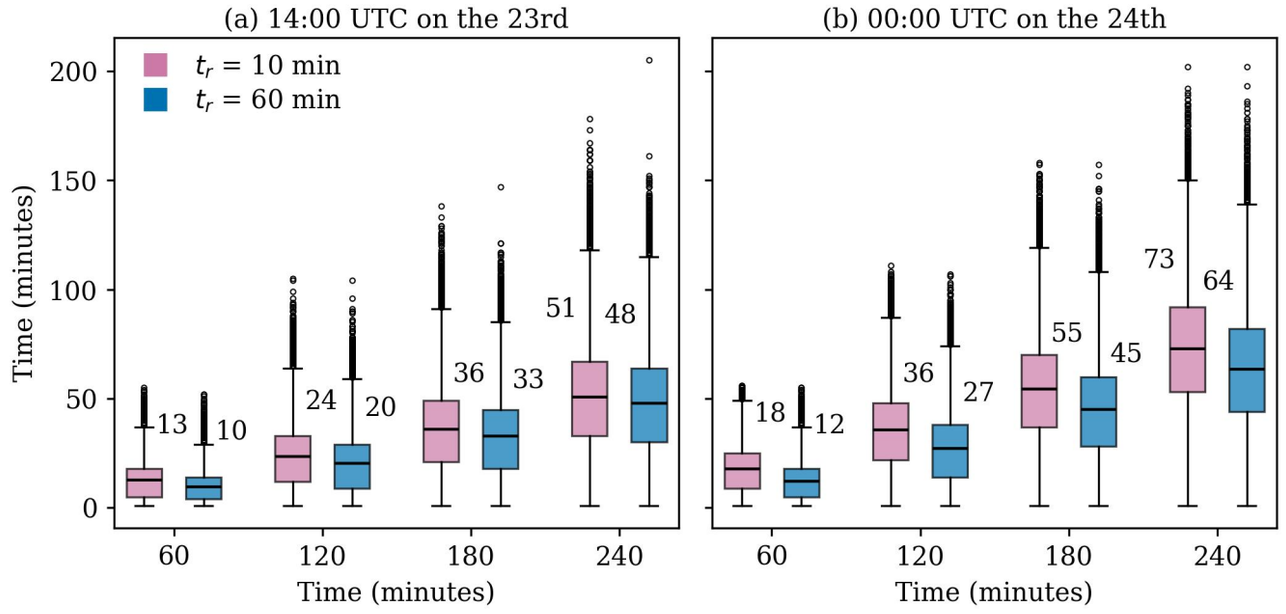



**Figure 7. Box plots of total in-cloud residence time of turbulent parcels for different analysis periods (60, 120, 180, and 240 min). (a) 14:00 UTC on the 23rd (LWP minimum), (b) 00:00 UTC on the 24th (strongest overall transport to the cloud base). Reddish purple boxes represent $t_r$ = 10 min, blue boxes represent $t_r$ = 60 min. The central black horizontal line represents the mean, computed only over parcels that entered the cloud (numerical values are labeled above each box), while the boxes represent the IQR. Whiskers extend to the maximum and minimum values within the non-outlier range. Black open circles represent outliers, defined as data points exceeding 1.5 times the IQR from the box edges.**

The results presented above focus on domain d02 with a grid spacing of 900 m. Furthermore, we compare the simulation results from the nested domains d02, d03, and d04 to evaluate how spatial resolution influences the instantaneous arrival rate, cumulative arrival rate, and transport time of turbulent parcels from the sea surface to the cloud base, as well as their residence time within the clouds. To ensure consistent cross-resolution comparisons, d02 and d03 are cropped to match the smaller d04 domain, and the analysis is limited to the first 90 min, during which at least 70 % of parcels remain within the domain across all release times, durations, and resolutions.

As the horizontal grid spacing decreases from d02 to d04, the peak instantaneous arrival rate decreases systematically for both release durations. For 10-min releases, the difference between the highest and lowest peak instantaneous arrival rates across the five release times decreases from 0.78 to 0.34 and 0.22 percentage points in d02, d03, and d04, respectively. For 60-min releases, this difference remains small across all three domains, ranging from 0.11 to 0.14 percentage points (Fig. 8, Table 3).



删除[Pan Zhao]: **8**
删除[Pan Zhao]: **simulation durations**
删除[Pan Zhao]: **Red**
删除[Pan Zhao]: <math>**, green**
删除[Pan Zhao]: <math>**.**
删除[Pan Zhao]: **median**
删除[Pan Zhao]: As d04 has the smallest spatial extent an
删除[Pan Zhao]: consistency and fair comparison across
删除[Pan Zhao]: geographic extent of
删除[Pan Zhao]: was restricted
删除[Pan Zhao]: minutes. During this period,
删除[Pan Zhao]: the
删除[Pan Zhao]: remained
删除[Pan Zhao]: for
删除[Pan Zhao]: release
删除[Pan Zhao]: gradually
删除[Pan Zhao]: monotonically
删除[Pan Zhao]: time of peak arrival is gradually delayed,
删除[Pan Zhao]: the cumulative arrival rate also shows a
删除[Pan Zhao]: for
删除[Pan Zhao]: are 3.39%, 2.28%, and 1.86%,
删除[Pan Zhao]: ; the corresponding peak arrival times ar
删除[Pan Zhao]: ; and the cumulative arrival rates are 94.
删除[Pan Zhao]: 9
删除[Pan Zhao]: 1). This pattern likely reflects two factor

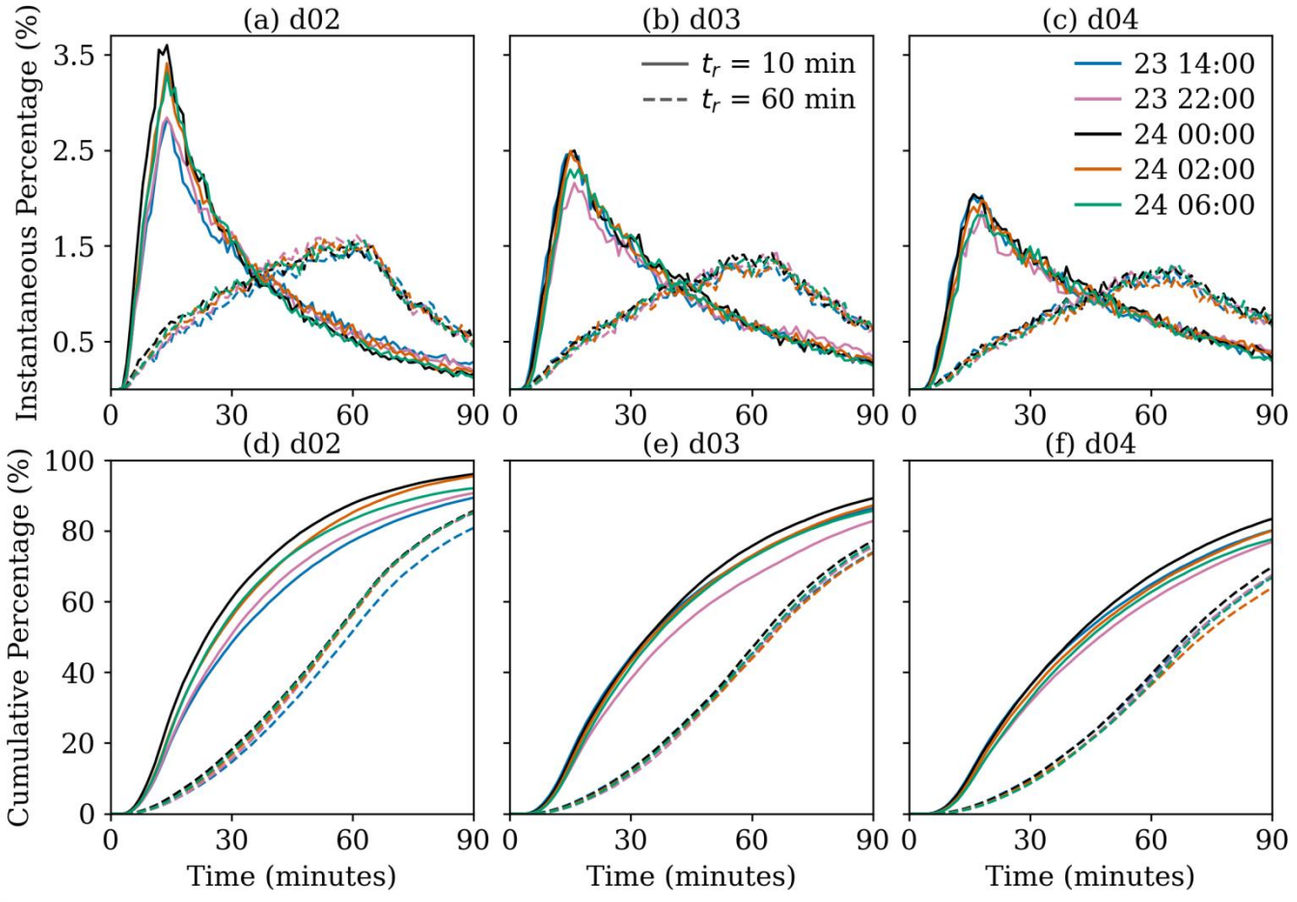



**Figure 8. Comparison of the instantaneous and cumulative arrival of turbulent parcels at the cloud base across different spatial resolutions (d02, d03, d04). Panels (a)-(c) show the instantaneous arrival rate, i.e., the percentage of turbulent parcels first reaching the cloud base per minute. Panels (d)-(f) show the corresponding cumulative arrival rate. Results are presented for five representative release times under two release configurations ($t_r$ = 10 min as solid lines, $t_r$ = 60 min as dashed lines). All d02 and d03 data have been cropped to the geographical extent of d04. Colors distinguish release times, blue (14:00 UTC on the 23rd), reddish purple (22:00 UTC on the 23rd), black (00:00 UTC on the 24th), vermillion (02:00 UTC on the 24th), and bluish green (06:00 UTC on the 24th).**

The cumulative arrival rate quantifies parcel delivery to cloud base over time. For the 00:00 UTC release on 24 September, cumulative arrivals decrease from 96.02 % (d02) to 89.18 % (d03) and 83.35 % (d04) within the 90-min, d04-cropped framework (Fig. 8, Table 3). Extending the integration to 120 min and expanding the domain to d03 reduces the d02 – d03 differences from 3.03 – 11.59 to 2.25 – 7.93 percentage points across five release times and both release durations (Table 3). Unlike instantaneous quantities, the cumulative arrival rates reflect the combined effects of model resolution, domain size,

删除[Pan Zhao]:
删除[Pan Zhao]: **9**
删除[Pan Zhao]: <math>
删除[Pan Zhao]: <math>
设置格式[Pan Zhao]: 字体: 加粗, 英语(英国)
删除[Pan Zhao]: **23rd**
设置格式[Pan Zhao]: 字体: 加粗, 英语(英国)
删除[Pan Zhao]: **), orange (**
设置格式[Pan Zhao]: 字体: 加粗, 英语(英国)
删除[Pan Zhao]:
设置格式[Pan Zhao]: 字体: 加粗, 英语(英国)
删除[Pan Zhao]: **), red (24th**
设置格式[Pan Zhao]: 字体: 加粗, 英语(英国)
删除[Pan Zhao]: **), green (**
设置格式[Pan Zhao]: 字体: 加粗, 英语(英国)
删除[Pan Zhao]:
设置格式[Pan Zhao]: 字体: 加粗, 英语(英国)
设置格式[Pan Zhao]: 字体: 加粗, 英语(英国)
删除[Pan Zhao]: **purple (24th**
设置格式[Pan Zhao]: 字体: 加粗, 英语(英国)
设置格式[Pan Zhao]: 字体: 加粗, 英语(英国)
删除[Pan Zhao]:
删除[Pan Zhao]: trajectories becomes weaker, thereby
删除[Pan Zhao]: .

and tracking duration, highlighting the importance of spatial and temporal sampling constraints when estimating aerosol delivery for MCB applications.

To explain the differences in instantaneous arrival rates across grid spacings, Fig. 9 compares the characteristics of vertical velocity distributions at different horizontal resolutions. We decompose $w$ into a 20-point moving average ($\overline{w}_{20pt}$) and a residual component in Figs. 9a-b. Higher resolution leads to lower $\overline{w}_{20pt}$, whereas resolution has only a minimal effect on the residual component, indicating that the weaker $w$ in the higher-resolution simulations is primarily attributable to changes in the mean state rather than in the fluctuations. Figures 9c-d show that, within each simulation, the fraction of turbulent parcels embedded in background ascending environments generally decreases with time, whereas the fraction embedded in background subsiding environments increases. The ascending fraction is slightly higher in d04 than in d02 and d03 during most of the analysis period. Figure 9e shows stronger subsidence in the lower and middle layers and weaker positive $w$ aloft in the high-resolution domain than in the low-resolution domain. Figure 9f shows stronger horizontal divergence in the lower boundary layer and stronger horizontal convergence aloft at higher resolutions, consistent with the vertical-velocity structure in Fig. 9e. Together, these results suggest that instantaneous arrival rates are modulated by the mean w and divergence along parcel trajectories, whereas the fraction of updrafts shows no clear relationship with arrival rates.

删除[Pan Zhao]: <math>
删除[Pan Zhao]: <math>
删除[Pan Zhao]: 10a
删除[Pan Zhao]: <math>
删除[Pan Zhao]: <math>
删除[Pan Zhao]: 10c
删除[Pan Zhao]: further
删除[Pan Zhao]: with increasing resolution
删除[Pan Zhao]: a
删除[Pan Zhao]: environment
删除[Pan Zhao]: a
删除[Pan Zhao]: environment
删除[Pan Zhao]: This suggests that, at
删除[Pan Zhao]: resolutions, parcels are less frequently sustained within background ascent.
删除[Pan Zhao]: 10e
删除[Pan Zhao]: <math>
删除[Pan Zhao]: 10f indicates
删除[Pan Zhao]: below 1 km
删除[Pan Zhao]: which is
删除[Pan Zhao]: shown
删除[Pan Zhao]: 10e
设置格式[Pan Zhao]: 题注，左

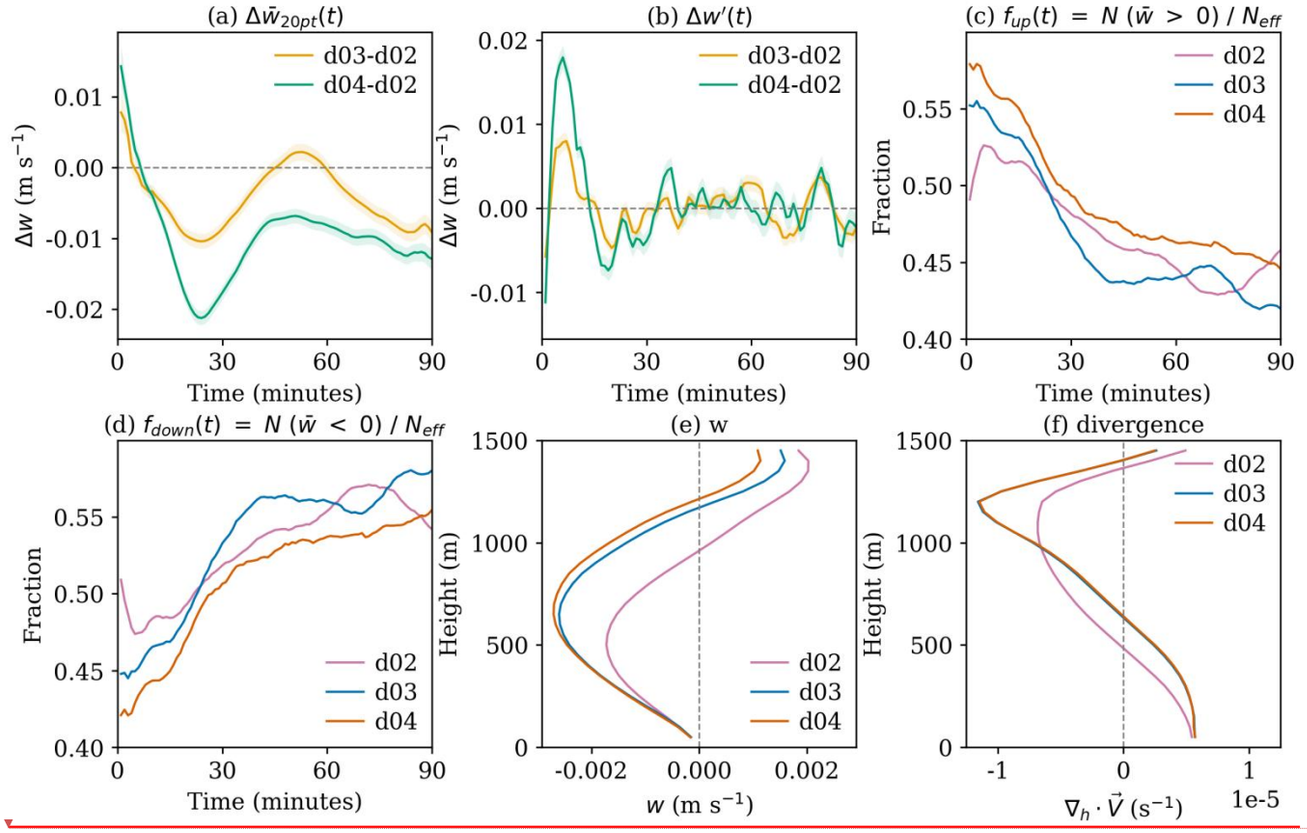



**Figure 9. Vertical transport characteristics and dynamic environmental parameters under different horizontal resolutions. Results are based on the first 90 minutes of simulation starting from 00:00 UTC on the 24th ($t_r$ = 10 min). All domain data are cropped to the d04 range for calculation. (a) Difference in the trajectory-sampled background $w$, $\Delta\bar{w}_{20pt}(t)$, where $\bar{w}_{20pt}(t)$ is the background component obtained from a 20-point centered running mean of the trajectory-sampled $w$. (b) Difference in the perturbation $w$, $\Delta w'(t)$. (c) Fraction of parcels in sustained positive background motion, $f_{up}(t) = N(\bar{w} > 0) / N_{eff}$. (d) Fraction of parcels in persistent negative background motion, $f_{down}(t) = N(\bar{w} < 0) / N_{eff}$, where $N_{eff}$ denotes the number of valid parcels at each time. (e) Vertical profile of w. (f) Vertical profiles of horizontal convergence (-) /divergence (+). Negative values on the x-axis represent horizontal convergence, and positive values represent horizontal divergence. The horizontal axis includes an order-of-magnitude scaling factor of $10^{-5}$. Color coding: In panels (a)-(b), d03 - d02 and d04 - d02 are shown in orange and bluish green, respectively. In panels (c)-(f), d02, d03, and d04 are shown in reddish purple, blue, and vermillion, respectively.**

删除[Pan Zhao]: Second, the limitations of simulation duration and domain size further amplify the transport differences among resolutions. When we extend the analysis window to 120 min and expand the spatial coverage to that of domain d03, the cumulative arrival rates increase markedly

删除[Pan Zhao]: **10**

删除[Pan Zhao]: <math>**).**

删除[Pan Zhao]: <math>, <math>,

删除[Pan Zhao]: <math>

删除[Pan Zhao]: <math>

删除[Pan Zhao]: <math>, <math>.

删除[Pan Zhao]: <math>.

删除[Pan Zhao]: <math>

删除[Pan Zhao]: <math>

删除[Pan Zhao]: <math> **vertical**

删除[Pan Zhao]: **. (f) Convergence / Divergence vertical profile.**

删除[Pan Zhao]: **end of the**

删除[Pan Zhao]: **is annotated with**

删除[Pan Zhao]: <math>.

设置格式[Pan Zhao]: 字体: 小五, 加粗, 英语(美国)

设置格式[Pan Zhao]: 正文, 左, 行距: 单倍行距

**Table 3. Parcel transport statistics for $t_r$ = 10 min and 60 min releases across simulation domains and release times, focusing on the first 90 or 120 min. Statistics include the peak instantaneous arrival rate, peak arrival time, and cumulative arrival rate at the end of the analysis period. For 90-min analyses, all domains are cropped to d04; for 120-min analyses, d02 and d03 are cropped to d03.**

| Domain | Release timing (UTC) | Analysis period (min) | Peak (%) | Peak time (min) | Final cumulative (%) | Peak (%) | Peak time (min) | Final cumulative (%) | Cropped to |
|---|---|---|---|---|---|---|---|---|---|
| | | | $t_r$ = 10 min | | | $t_r$ = 60 min | | | |
| d02 | 23 14:00 | 90 | 2.82 | 14 | 89.38 | 1.50 | 61 | 80.80 | d04 |
| | 23 22:00 | 90 | 2.84 | 14 | 90.64 | 1.61 | 61 | 84.97 | d04 |
| | 24 00:00 | 90 | 3.60 | 14 | 96.02 | 1.56 | 60 | 85.59 | d04 |
| | 24 02:00 | 90 | 3.41 | 14 | 95.44 | 1.57 | 53 | 85.26 | d04 |
| | 24 06:00 | 90 | 3.31 | 14 | 92.04 | 1.56 | 59 | 85.10 | d04 |
| d03 | 23 14:00 | 90 | 2.47 | 15 | 86.35 | 1.31 | 55 | 73.89 | d04 |
| | 23 22:00 | 90 | 2.16 | 16 | 82.72 | 1.45 | 66 | 75.44 | d04 |
| | 24 00:00 | 90 | 2.50 | 16 | 89.18 | 1.42 | 65 | 77.16 | d04 |
| | 24 02:00 | 90 | 2.49 | 15 | 87.14 | 1.35 | 66 | 73.67 | d04 |
| | 24 06:00 | 90 | 2.30 | 17 | 85.64 | 1.38 | 64 | 76.19 | d04 |
| d04 | 23 14:00 | 90 | 2.02 | 18 | 80.14 | 1.24 | 64 | 67.07 | d04 |
| | 23 22:00 | 90 | 1.86 | 18 | 76.86 | 1.28 | 66 | 67.51 | d04 |
| | 24 00:00 | 90 | 2.04 | 16 | 83.35 | 1.26 | 63 | 69.77 | d04 |
| | 24 02:00 | 90 | 1.98 | 18 | 80.04 | 1.16 | 66 | 63.94 | d04 |
| | 24 06:00 | 90 | 1.82 | 17 | 77.59 | 1.29 | 65 | 66.77 | d04 |
| d02 | 23 14:00 | 120 | 2.82 | 14 | 94.88 | 1.50 | 61 | 91.78 | d03 |
| | 23 22:00 | 120 | 2.84 | 14 | 95.50 | 1.61 | 61 | 94.79 | d03 |
| | 24 00:00 | 120 | 3.60 | 14 | 98.72 | 1.56 | 60 | 95.29 | d03 |
| | 24 02:00 | 120 | 3.41 | 14 | 98.44 | 1.57 | 53 | 95.06 | d03 |
| | 24 06:00 | 120 | 3.31 | 14 | 96.08 | 1.56 | 59 | 94.63 | d03 |
| d03 | 23 14:00 | 120 | 2.47 | 15 | 92.63 | 1.31 | 55 | 87.43 | d03 |
| | 23 22:00 | 120 | 2.16 | 16 | 90.78 | 1.45 | 66 | 89.01 | d03 |
| | 24 00:00 | 120 | 2.50 | 16 | 95.17 | 1.42 | 65 | 90.57 | d03 |
| | 24 02:00 | 120 | 2.49 | 15 | 93.76 | 1.35 | 66 | 87.13 | d03 |
| | 24 06:00 | 120 | 2.30 | 17 | 93.58 | 1.38 | 64 | 89.79 | d03 |

In addition to the instantaneous and cumulative arrival rates, we investigate the sensitivity of in-cloud residence time to horizontal grid spacing. Figure 10 presents the boxplots of in-cloud residence time for the d02, d03, and d04 domains at two representative release times (14:00 UTC on the 23rd and 00:00 UTC on the 24th) for the $t_r$ = 10 min group within the d04-cropped 90-min framework. Within this framework, the results indicate that decreasing grid spacing leads to a reduction in in-cloud residence time. For the release at 00:00 UTC on the 24th, the mean residence time is 27 min in d02, which decreases to 22 min in d03 and further to 19 min in d04. Enhanced TKE at the cloud top likely contributes to this accelerated venting of parcels from the cloud.



删除[Pan Zhao]: **1. Statistics of parcel**

删除[Pan Zhao]: **characteristics under different**

删除[Pan Zhao]: **,**

删除[Pan Zhao]: **and simulation durations (<math>).**

删除[Pan Zhao]: **final**

删除[Pan Zhao]: **.**

删除[Pan Zhao]: **simulations,**

删除[Pan Zhao]: **d02, d03, and d04**

删除[Pan Zhao]: **all**

删除[Pan Zhao]: **the domain size of**

删除[Pan Zhao]: **simulations**

删除[Pan Zhao]: **the domain size of d03; and the full**

设置格式[Pan Zhao]: 字体: 加粗

删除[Pan Zhao]: Start Time

删除[Pan Zhao]: Simulation Duration

删除[Pan Zhao]: Focused Area

删除[Pan Zhao]: Time

删除[Pan Zhao]: Cumulative

设置格式[Pan Zhao]: 字体: 小五, 非加粗, 英语(美国)

设置格式[Pan Zhao]: 正文, 居中, 行距: 单倍行距, 无

设置格式[Pan Zhao]: 字体: 小五, 非加粗, 英语(美国)

设置格式[Pan Zhao]: 字体: 小五, 非加粗, 英语(美国)

设置格式[Pan Zhao]: 字体: 小五, 非加粗, 英语(美国)

设置格式[Pan Zhao]: 正文, 居中, 行距: 单倍行距, 无

设置格式[Pan Zhao]: 字体: 小五, 非加粗, 英语(美国)

设置格式[Pan Zhao]: 字体: 小五, 非加粗, 英语(美国)

设置格式[Pan Zhao]: 字体: 小五, 非加粗, 英语(美国)

设置格式[Pan Zhao]: 字体: 小五, 非加粗, 英语(美国)

The resolution dependence of parcel transport is consistent with previous LES studies highlighting the importance of resolved turbulent transport pathways for near-surface aerosol delivery (Dhandapani et al., 2025). Previous simulations and observations also demonstrate the roles of plume dispersion and meteorological conditions in transporting aerosols toward cloud base (McMichael et al., 2024; Kainz et al., 2026; Hernandez-Jaramillo et al., 2025). Although differences in transport metrics and experimental configurations preclude direct quantitative comparisons, our results are qualitatively consistent with these studies and provide complementary Lagrangian constraints on surface-to-cloud transport, without explicitly resolving aerosol dispersion or microphysical processes.

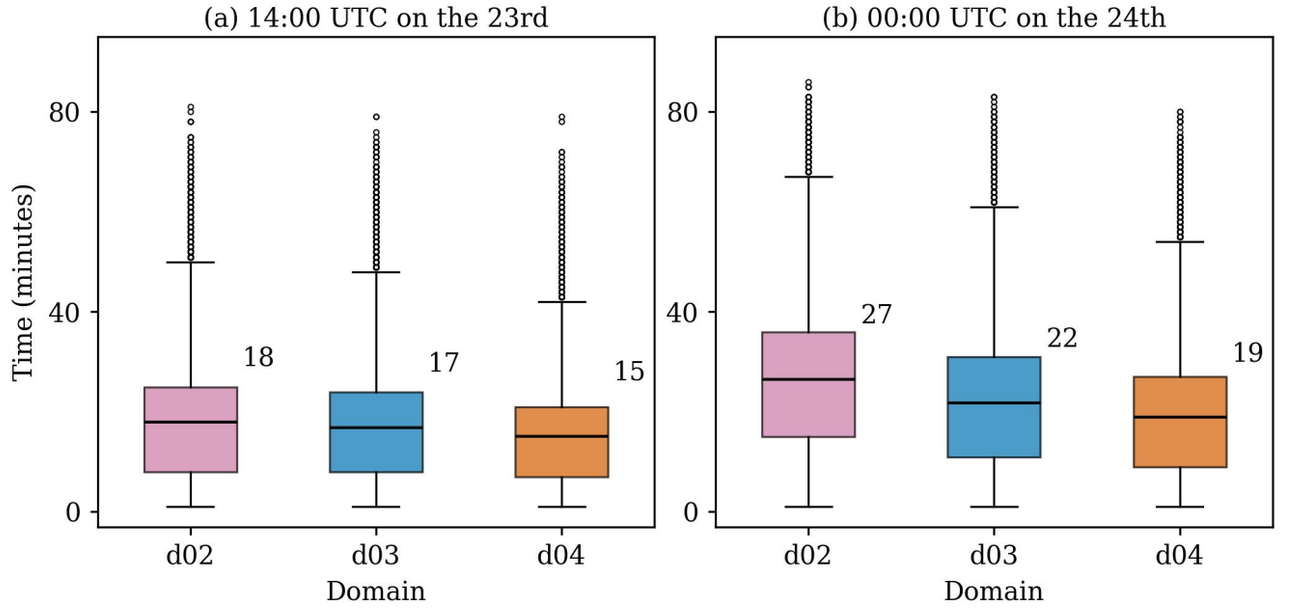



**Figure 10. Boxplot statistics of in-cloud residence time across d02, d03, and d04 domains. Panels (a) and (b) correspond to the release times at 14:00 UTC on the 23rd and 00:00 UTC on the 24th, respectively, for the $t_r$ = 10 min group within a 90-min window. The reddish purple, blue, and vermillion boxes represent results from the d02, d03, and d04 domains, respectively. For consistency in spatial comparison, all data from the d02 and d03 domains are cropped to match the geographical extent of the d04 domain. The central black horizontal line represents the mean, computed only over parcels that entered the cloud (numerical values are labeled above each box), while the boxes represent the IQR. Whiskers extend to the maximum and minimum values within the non-outlier range. Black open circles represent outliers, defined as data points exceeding 1.5 times the IQR from the box edges.**

### 3.4 Implications for Droplet Activation

In addition to transport efficiency and in-cloud residence time, quantifying the activation fraction (AF) at cloud base is necessary to close the pathway from sea-surface aerosol emissions to cloud droplet formation, particularly under turbulent

删除[Pan Zhao]: These results indicate that parcel transport to the cloud base, as characterized by the instantaneous arrival rate and cumulative arrival rate, is jointly regulated by release duration, LWP evolution stage, and horizontal resolution, with significant differences in in-cloud residence time. These

设置格式[Pan Zhao]: 字体: 加粗, （中文）中文(简体)

删除[Pan Zhao]: **11**

设置格式[Pan Zhao]: 字体: 加粗, （中文）中文(简体)

删除[Pan Zhao]: <math>

设置格式[Pan Zhao]: 字体: 加粗, （中文）中文(简体)

设置格式[Pan Zhao]: 字体: 加粗, （中文）中文(简体)

删除[Pan Zhao]: **, green,**

设置格式[Pan Zhao]: 字体: 加粗, （中文）中文(简体)

删除[Pan Zhao]: **red**

设置格式[Pan Zhao]: 字体: 加粗, （中文）中文(简体)

删除[Pan Zhao]: **median**

设置格式[Pan Zhao]: 字体: 加粗, （中文）中文(简体)

设置格式[Pan Zhao]: 正文

删除[Pan Zhao]:

删除[Pan Zhao]: AF

conditions. Here, AF is derived from cloud-base vertical velocities and represents the conditional activation fraction of parcels reaching cloud base, rather than the overall activation efficiency of aerosols released near the ocean surface. FLEXPART-WRF is used solely to diagnose Lagrangian transport of turbulent air parcels, as no physical emission rate is prescribed (Sect. 2.5). Accordingly, cloud droplet activation is evaluated over a prescribed two-dimensional aerosol parameter space using the parameterization of Abdul-Razzak et al. (1998), rather than particle-derived three-dimensional concentration fields.

In the estimation of AF, the physicochemical properties of sea-salt aerosols are prescribed as follows: molar mass $M_a = 0.05844$ kg mol$^{-1}$, density $\rho_a = 2200$ kg m$^{-3}$ (Koepke et al., 1997; Hess et al., 1998), and geometric standard deviation $\sigma_g = 2.03$ (Koepke et al., 1997; Hess et al., 1998; Jaeglé et al., 2011). A two-dimensional 30×30 parameter space is constructed to cover a wide range of conditions, in which the geometric mean diameter ($D_g$) spans 0.02 – 5 μm with logarithmic spacing (Quinn et al., 2017), and the aerosol number concentration ($N_a$) ranges from 10 – 5000 cm$^{-3}$, representing both clean and polluted marine environments (Quinn et al., 2017; O'Dowd and de Leeuw, 2007).

We calculate AF using w, temperature (T), and pressure (P) sampled from Lagrangian particle trajectories over a 90-min period following release within the d04-cropped spatial domain. For each trajectory, the first point at which RH exceeds 100 % is identified as the reference level for the cloud-base activation layer, which extends 50 m above and below this level. A trajectory is classified as transport-qualified if a positive vertical velocity ($w > 0$) occurs within this layer, and the first such point is then used for the subsequent AF calculation. This procedure ensures that AF is evaluated only for parcels that both reach the cloud-base region and have upward motion favorable for activation. The sampled variables within the activation height range are then used to compute the activation fraction following Eq. (30) of Abdul-Razzak et al. (1998), written here as

$$\frac{N}{N_{ap}} = \frac{1}{2}\operatorname{erfc}\left\{\ln\left[f_1(\ln\sigma)\left(\frac{\zeta}{\eta}\right)^{\frac{3}{2}} + f_2(\ln\sigma)\left(\frac{S_m^2}{\eta + 3\zeta}\right)^{\frac{3}{4}}\right] \div (3\sqrt{2}\ln\sigma)\right\} \quad (1)$$

where $N/N_{ap}$ gives the conditional AF, N is the activated aerosol number concentration, $N_{ap}$ is the total aerosol number concentration, $S_m$ is the critical supersaturation corresponding to the geometric mean diameter, $\sigma$ is the geometric standard deviation of the aerosol size distribution, and $f_1$, $f_2$, $\eta$, and $\zeta$ are defined following Abdul-Razzak et al. (1998). In this study, for each prescribed ($D_g$, $N_a$) combination, the conditional AF is calculated for each activation-qualified trajectory and then averaged across all qualified trajectories to obtain the AF distribution shown in Fig. 11. For comparison across experiments,



删除[Pan Zhao]: The
删除[Pan Zhao]: used here
删除[Pan Zhao]: a
删除[Pan Zhao]: metric
删除[Pan Zhao]: a bulk fraction based on all
删除[Pan Zhao]: parcels. Specifically, AF represents the
删除[Pan Zhao]: aerosol conditions. To this end, we evaluate
删除[Pan Zhao]: widely adopted
删除[Pan Zhao]: and Ghan
删除[Pan Zhao]: ).
删除[Pan Zhao]: molecular weight <math>
删除[Pan Zhao]: <math>(
删除[Pan Zhao]: .
删除[Pan Zhao]: .
删除[Pan Zhao]: <math>
删除[Pan Zhao]: .
删除[Pan Zhao]: .
删除[Pan Zhao]: .
删除[Pan Zhao]: <math>
删除[Pan Zhao]: from <math>
删除[Pan Zhao]: .
删除[Pan Zhao]: <math>
删除[Pan Zhao]: <math>
删除[Pan Zhao]: <math>
删除[Pan Zhao]: <math>
删除[Pan Zhao]: minute
删除[Pan Zhao]: coverage of d04. The
删除[Pan Zhao]: is defined as the height range extending

the mean conditional AF in Table 4 is subsequently calculated by averaging the resulting AF values over the 900 prescribed ($D_g$, $N_a$) combinations.

For parcels reaching cloud base, the conditional AF increases with increasing $D_g$ and decreasing $N_a$ (Fig. 11a), consistent with reduced critical supersaturation for larger aerosols and enhanced supersaturation under lower aerosol loading (e.g., Chen et al., 2018). AF shows little sensitivity to release duration ($t_r$ = 60 min and $t_r$ = 10 min in Fig. 11b), but is higher for releases at 00:00 than for those at 14:00 (Fig. 11c), likely due to stronger cloud-base updrafts during periods of higher LWP (Fig. 12). AF also increases systematically with horizontal resolution (Fig. 11d), with maximum values ranging from 0.76 – 0.91 in d02, to 0.87 – 0.96 in d03 and 0.93 – 0.96 in d04. Similarly, mean AF across all 900 aerosol parameter combinations increases from 0.21 – 0.43 in d02 to 0.32 – 0.50 in d03 and 0.38 – 0.51 in d04 (Table 4). This enhancement likely reflects stronger cloud-base updrafts resolved at finer grid spacing (Fig. 12b), although its magnitude depends on the prescribed aerosol conditions.

Because conditional AF represents only parcels reaching cloud-base activation conditions, it does not account for the fraction of surface-released aerosols that reach cloud base. Multiplying the fraction of transported parcels by the mean conditional AF yields approximate joint transport–activation fractions of 0.12 – 0.28, 0.16 – 0.31, and 0.18 – 0.32 for d02, d03, and d04, respectively (Table 4). Although the joint fraction increases with resolution, it remains well below 0.5, highlighting that only a limited fraction of released aerosols may contribute to cloud droplet activation. These findings suggest caution when assuming that increased aerosol emissions translate directly into proportional increases in cloud droplet number concentration in MCB applications.



删除[Pan Zhao]: Overall

删除[Pan Zhao]: larger <math>

删除[Pan Zhao]: smaller

删除[Pan Zhao]: <math>

删除[Pan Zhao]: 12a). This trend is expected because larg

删除[Pan Zhao]: to activate, while lower <math> tends

删除[Pan Zhao]: , further enhancing the AF (

删除[Pan Zhao]: 2016,

删除[Pan Zhao]: Differences in AF between the two

删除[Pan Zhao]: durations (<math> and <math>) are

删除[Pan Zhao]: 12b). However, release timing has a not

删除[Pan Zhao]: leads to a higher AF

删除[Pan Zhao]: releasing

删除[Pan Zhao]: 12c). This indicates that injecting aeroso

删除[Pan Zhao]: because w is

删除[Pan Zhao]: at 00:00 (Fig. 13). High-

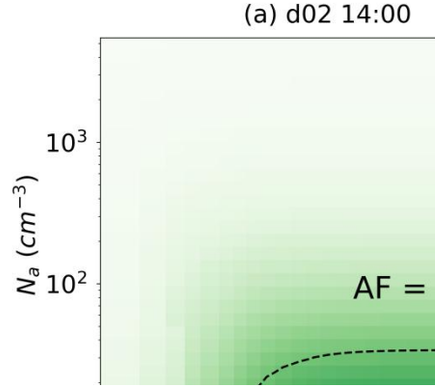
删除[Pan Zhao]: simulations yield a higher AF than low-

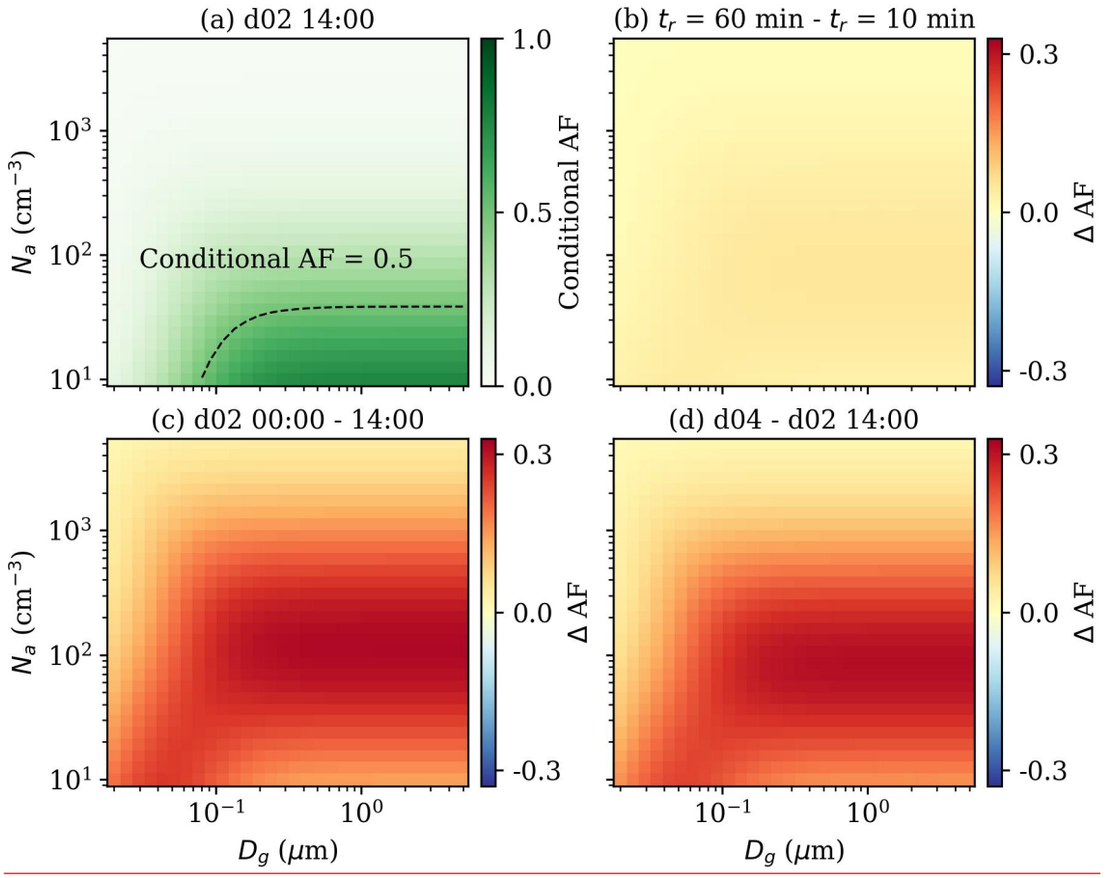
删除[Pan Zhao]: the coarse-resolution domain (

删除[Pan Zhao]: ) fluctuates between 0.73 and 0.91, wher

删除[Pan Zhao]: ) maintains a stable range of 0.92-0.96.

删除[Pan Zhao]: because higher resolution resolves highe






555

**Figure 11. Sensitivity of the conditional AF and its deviations (ΔAF) for single-mode sea-salt aerosols to grid resolution, release time, and release duration, shown as a function of aerosol $D_g$ and $N_a$. Here, AF is diagnosed only for the activation-qualified subset of turbulent parcels, i.e., parcels that reach the cloud-base activation layer and exhibit positive vertical velocity within this layer.** 560 **(a) Absolute AF distribution in d02 at 14:00 UTC on the 23rd for $t_r$=10 min; the black dashed line indicates the conditional AF = 0.5 contour. The "Greens" color scale represents AF values from 0 to 1. (b) ΔAF in d02 at 14:00 UTC on the 23rd between $t_r$ = 60 min and $t_r$ = 10 min. (c) ΔAF in d02 between 00:00 UTC on the 24th and 14:00 UTC on the 23rd for $t_r$ = 10 min. (d) ΔAF between d04 and d02 at 14:00 UTC on the 23rd. The "RdYlBu_r" color scale (red/blue for positive/negative deviations) represents differences in AF.**

删除[Pan Zhao]: **12**

删除[Pan Zhao]: <math>

删除[Pan Zhao]: <math>

删除[Pan Zhao]: <math>.

删除[Pan Zhao]: <math>

删除[Pan Zhao]: <math>

删除[Pan Zhao]: <math>

删除[Pan Zhao]: <math>

删除[Pan Zhao]: <math>

删除[Pan Zhao]: <math>.

删除[Pan Zhao]: <math>

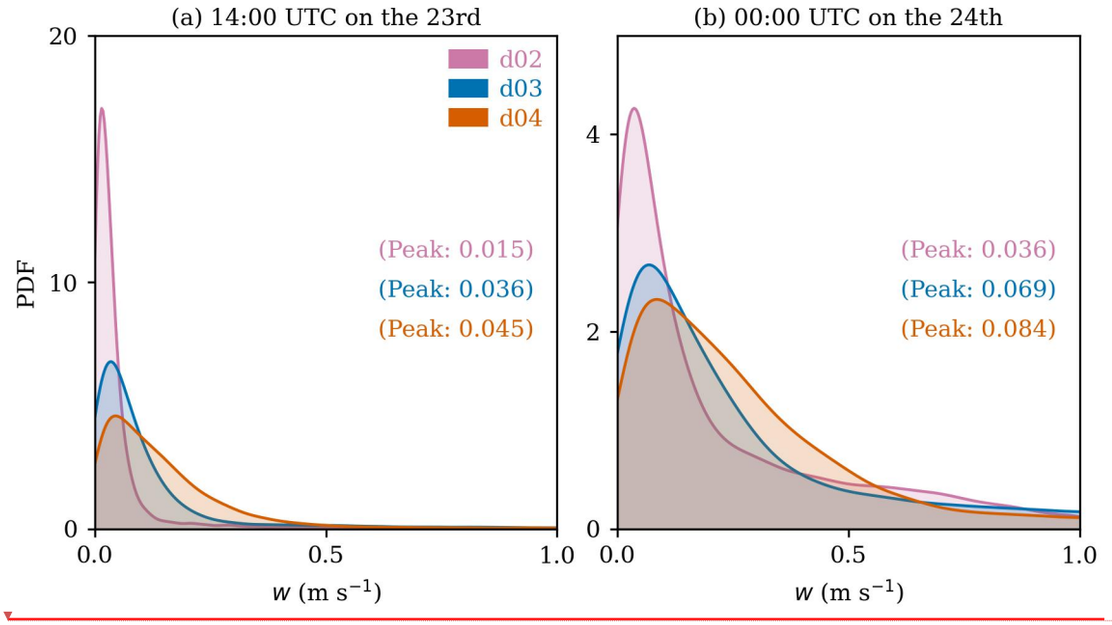



**Figure 12. PDFs of the sampled cloud-base $w$ used for activation diagnostics. (a) Comparison of w distributions across d02, d03, and d04 at 14:00 UTC on the 23rd ($t_r$ = 10 min); (b) Comparison of $w$ distributions at 00:00 UTC on the 24th ($t_r$ = 10 min). Values in parentheses indicate the peak positions of the respective PDF curves. Reddish purple, blue and vermillion curves represent the results for d02, d03, and d04, respectively.**

删除[Pan Zhao]:
设置格式[Pan Zhao]: （中文）中文(简体)
删除[Pan Zhao]: **13**
设置格式[Pan Zhao]: （中文）中文(简体)
删除[Pan Zhao]: <math>
设置格式[Pan Zhao]: （中文）中文(简体)
删除[Pan Zhao]: <math>
设置格式[Pan Zhao]: （中文）中文(简体)
删除[Pan Zhao]: <math>
设置格式[Pan Zhao]: （中文）中文(简体)
删除[Pan Zhao]: <math>**).**
设置格式[Pan Zhao]: （中文）中文(简体)
删除[Pan Zhao]: **Blue, green,**
设置格式[Pan Zhao]: （中文）中文(简体)
删除[Pan Zhao]: **red**
设置格式[Pan Zhao]: （中文）中文(简体)
删除[Pan Zhao]:

**Table 4. Summary of the transport-qualified fraction, mean conditional AF, and joint transport-activation metric for the five release times, three horizontal resolutions (d02, d03, and d04), and two release durations ($t_r$ = 10 min and $t_r$ = 60 min), based on a 90-min analysis period within the d04-cropped spatial domain. The transport-qualified fraction denotes the fraction of released turbulent parcels that reach the cloud-base activation layer and have positive vertical velocity at the first qualified point within the ±50 m layer. The mean conditional AF is averaged over the 900 prescribed ($D_g$, $N_a$) combinations. The joint metric is calculated as the product of the transport-qualified fraction and the mean conditional AF and is used as a diagnostic of the combined transport-activation pathway rather than as an absolute aerosol activation efficiency.**

| Domain | Release timing (UTC) | Transport-qualified fraction | Mean conditional AF | Joint metric | Transport-qualified fraction | Mean conditional AF | Joint metric |
|---|---|---|---|---|---|---|---|
| | | $t_r$ = 10 min | | | $t_r$ = 60 min | | |
| d02 | 23 14:00 | 0.55 | 0.21 | 0.12 | 0.48 | 0.24 | 0.12 |
| | 23 22:00 | 0.60 | 0.35 | 0.21 | 0.55 | 0.38 | 0.21 |
| | 24 00:00 | 0.71 | 0.40 | 0.28 | 0.58 | 0.39 | 0.23 |
| | 24 02:00 | 0.69 | 0.40 | 0.28 | 0.57 | 0.39 | 0.22 |
| | 24 06:00 | 0.59 | 0.43 | 0.25 | 0.54 | 0.40 | 0.22 |
| d03 | 23 14:00 | 0.61 | 0.32 | 0.20 | 0.48 | 0.33 | 0.16 |
| | 23 22:00 | 0.59 | 0.45 | 0.27 | 0.52 | 0.46 | 0.24 |
| | 24 00:00 | 0.68 | 0.46 | 0.31 | 0.56 | 0.48 | 0.27 |
| | 24 02:00 | 0.66 | 0.47 | 0.31 | 0.52 | 0.47 | 0.24 |
| | 24 06:00 | 0.62 | 0.50 | 0.31 | 0.53 | 0.50 | 0.27 |
| d04 | 23 14:00 | 0.61 | 0.38 | 0.23 | 0.47 | 0.39 | 0.18 |
| | 23 22:00 | 0.57 | 0.48 | 0.27 | 0.50 | 0.49 | 0.25 |
| | 24 00:00 | 0.67 | 0.48 | 0.32 | 0.54 | 0.49 | 0.26 |
| | 24 02:00 | 0.63 | 0.48 | 0.30 | 0.47 | 0.48 | 0.23 |
| | 24 06:00 | 0.57 | 0.51 | 0.29 | 0.47 | 0.50 | 0.24 |

## 4 Conclusions

This study investigates the transport of turbulent parcels from the ocean surface to the cloud base and its implications for cloud droplet activation in a Southeast Atlantic stratocumulus case. We decompose this pathway into the transport fraction reaching cloud base and the activation fraction from cloud-base aerosols to cloud droplets. By coupling WRF-LES with the FLEXPART-WRF Lagrangian dispersion model, we quantify the transport characteristics of turbulent parcels from the sea surface to the cloud base, including the instantaneous arrival rate, cumulative arrival rate, transport time, in-cloud residence time, and the potential implications of these transport pathways for cloud droplet activation. The main findings are as follows:

(1) The thermodynamic structure of the boundary layer in the study region is generally uniform; however, turbulence intensity varies markedly across different stages of LWP evolution. Stronger boundary-layer turbulent mixing occurs during the LWP peak and rapid-growth phase. The timing of turbulent parcel release influences the height and thickness of the

删除[Pan Zhao]: key uncertainties

删除[Pan Zhao]: MCB feasibility, focusing on

删除[Pan Zhao]: typical stratocumulus region in the tropical

删除[Pan Zhao]: .

删除[Pan Zhao]: particle

删除[Pan Zhao]: The four-level one-way nested WRF simulation (grid spacing from 2.7 km to 100 m) effectively reproduces the spatiotemporal distribution and evolutionary characteristics of LWP in the study area. The results show good agreement with MODIS satellite observations and significantly mitigate the underestimation of marine stratocumulus LWP in ERA5 reanalysis, thereby providing a reliable meteorological background for the subsequent Lagrangian particle trajectory analysis.

设置格式[Pan Zhao]: 无项目符号或编号

supersaturated layer as well as the TKE experienced by the parcels, thereby modulating their transport to the cloud base and the subsequent activation conditions.

(2) Turbulent parcel transport to the cloud base, as characterized by the instantaneous arrival rate and cumulative arrival rate, is jointly controlled by release duration, release timing, and horizontal resolution. Short-pulse releases ($t_r$ = 10 min) produce higher peak instantaneous arrival rates, whereas continuous releases ($t_r$ = 60 min) are characterized by lower peaks and more delayed arrival times; overall transport to the cloud base is strongest during the rapid-growth stage of LWP. As the horizontal resolution increases from d02 (900 m) to d04 (100 m), the peak instantaneous arrival rate decreases, and the cumulative arrival rate diagnosed within the analyzed window also decreases overall. This is mainly because the background mean ascent experienced by the parcels weakens at higher resolution, while the truncation effect associated with finite integration time and domain size becomes stronger for slowly rising parcels, thereby jointly reducing the diagnosed overall transport to the cloud base within the analyzed window.

(3) In-cloud residence time and cloud-base activation processes are also sensitive to model resolution. Strong turbulence and abundant water vapor favor longer in-cloud residence times of turbulent parcels. With increasing resolution, the average in-cloud residence time shortens. Based on simplified single-mode sea-salt aerosol experiments, for the subset of parcels that reach the cloud-base activation layer and exhibit positive vertical velocity within this layer, the conditional AF increases with increasing particle size and decreasing aerosol number concentration, while showing little sensitivity to release duration. The maximum conditional AF increases from 0.76 – 0.91 in d02 to 0.87 – 0.96 in d03 and 0.93 – 0.96 in d04, whereas the mean conditional AF across the prescribed aerosol parameter space ranges from 0.21 – 0.43, 0.32 – 0.50, and 0.38 – 0.51, respectively.

(4) Multiplying the transport-qualified fraction by the mean conditional AF yields approximate joint transport–activation fractions of 0.12 – 0.28 in d02, 0.16 – 0.31 in d03, and 0.18 – 0.32 in d04. This metric provides a diagnostic of the combined transport and activation pathway, but it cannot be interpreted as a direct estimate of the fraction of physically emitted MCB aerosols that activate, because FLEXPART-WRF in air-parcel mode tracks air parcels rather than individual aerosol particles, and the conditional AF is calculated using prescribed aerosol properties and a simplified activation parameterization rather than a fully coupled aerosol–cloud simulation.

In summary, this study characterizes the Lagrangian transport of turbulent parcels from the sea surface to the cloud base and examines how release conditions, model resolution, and cloud dynamics regulate their transport and activation, providing process-level constraints on aerosol delivery for MCB. The analysis is limited to a single non-precipitating case, motivating future studies across broader regions, seasons, and meteorological conditions. Because FLEXPART-WRF tracks passive turbulent parcels without explicitly representing aerosol-specific processes, the diagnosed transport efficiency reflects air-

删除[Pan Zhao]: <math>

删除[Pan Zhao]: <math>

删除[Pan Zhao]: stronger

删除[Pan Zhao]: LWP peak and

删除[Pan Zhao]: stages than during low-LWP periods

删除[Pan Zhao]: the peak arrival time is delayed,

删除[Pan Zhao]: limited

删除[Pan Zhao]: and later-arriving

删除[Pan Zhao]: , yet extreme long-residence events become more frequent.

删除[Pan Zhao]: droplet

删除[Pan Zhao]: significantly

删除[Pan Zhao]: remaining insensitive

删除[Pan Zhao]: High-resolution simulations yield higher

删除[Pan Zhao]: because they better resolve strong cloud-base updrafts.

删除[Pan Zhao]: In summary, this study reveals, from a Lagrangian viewpoint, the transport characteristics of turbulent parcels from the sea surface to the cloud base within the marine boundary layer, as well as the modulating effects of release conditions, horizontal resolution, and in-cloud

parcel transport rather than actual aerosol delivery. Future comparisons with passive-tracer simulations in WRF and with explicit aerosol/plume simulations using WRF-Chem could help distinguish uncertainties in turbulent transport from aerosol-specific effects. Larger or periodic domains could reduce lateral parcel loss and sampling limitations, while multimodal aerosol representations and cloud parcel model simulations that resolve supersaturation and droplet growth over the in-cloud residence time could better constrain the full MCB transport–activation pathway.

## Code and data availability

The ERA5 reanalysis data used in this study are available from the Copernicus Climate Data Store (https://cds.climate.copernicus.eu/). The MODIS satellite data were obtained from the National Aeronautics and Space Administration (NASA) via their official data portal (https://modis.gsfc.nasa.gov/). The FLEXPART-WRF model code employed for Lagrangian particle dispersion simulations is publicly accessible at the NILU Git repository (https://git.nilu.no/flexpart/flexpart-wrf/). A subset of analyzed data and post-processing Python code are also available from Zenodo (https://zenodo.org/records/20394773).

删除[Pan Zhao]: python

## Author contributions

Conceptualization: Jingyi Chen

Data curation: Pan Zhao, Jingyi Chen

Formal analysis: Jingyi Chen, Pan Zhao

Funding acquisition: Yang Yang, Jingyi Chen

Investigation: Pan Zhao, Jingyi Chen

Methodology: Jingyi Chen, Pan Zhao

Project administration: Jingyi Chen, Yang Yang

Resources: Yue Jia, Pan Zhao, Jingyi Chen, Yang Yu

删除[Pan Zhao]: Yu

Software: Pan Zhao, Jingyi Chen, Yue Jia

Supervision: Jingyi Chen

Validation: Pan Zhao, Jingyi Chen, Yang Yang

Visualization: Pan Zhao

Writing (original draft preparation): Pan Zhao

Writing (review and editing): Jingyi Chen, Yang Yang, Yue Jia

## Competing interests

The authors declare that they have no competing interests.

## Acknowledgements

We acknowledge the High-Performance Computing Center of Nanjing University of Information Science & Technology for its support of this work. We thank Colleen Kaul for insightful discussions and inspiring perspectives on this topic.

## Financial support

This study is supported by the National Key Research and Development Program of China (grant 2024YFF0811400), the National Natural Science Foundation of China (Grant No. 42405076), the Startup Foundation for Introducing Talent of NUIST (Grant No. 2024r099), and the Distinguished Young Scholars Program of the National Natural Science Foundation of China (Overseas).

## References

Abdul-Razzak, H., Ghan, S. J., and Rivera-Carpio, C.: A parameterization of aerosol activation: 1. Single aerosol type, J. Geophys. Res. Atmos., 103, 6123–6131, https://doi.org/10.1029/97JD03735, 1998.

Abdul-Razzak, H. and Ghan, S. J.: A parameterization of aerosol activation: 2. Multiple aerosol types, J. Geophys. Res. Atmos., 105, 6837–6844, https://doi.org/10.1029/1999JD901161, 2000.

Ahlm, L., Jones, A., Stjern, C. W., Muri, H., Kravitz, B., and Kristjánsson, J. E.: Marine cloud brightening – as effective without clouds, Atmos. Chem. Phys., 17, 13071–13087, https://doi.org/10.5194/acp-17-13071-2017, 2017.

Arbizu-Barrena, C., Pozo-Vázquez, D., Ruiz-Arias, J. A., and Tovar-Pescador, J.: Macroscopic cloud properties in the WRF NWP model: An assessment using sky camera and ceilometer data, J. Geophys. Res. Atmos., 120, 10297–10312, https://doi.org/10.1002/2015JD023502, 2015.

Bower, K., Choularton, T., Latham, J., Sahraei, J., and Salter, S.: Computational assessment of a proposed technique for global warming mitigation via albedo-enhancement of marine stratocumulus clouds, Atmos. Res., 82, 328–336, https://doi.org/10.1016/j.atmosres.2005.11.013, 2006.

Brioude, J., Arnold, D., Stohl, A., Cassiani, M., Morton, D., Seibert, P., Angevine, W., Evan, S., Dingwell, A., Fast, J. D., Easter, R. C., Pisso, I., Burkhart, J., and Wotawa, G.: The Lagrangian particle dispersion model FLEXPART-WRF version 3.1, Geosci. Model Dev., 6, 1889–1904, https://doi.org/10.5194/gmd-6-1889-2013, 2013.

Chen, J., Liu, Y., Zhang, M., and Peng, Y.: Height Dependency of Aerosol-Cloud Interaction Regimes, J. Geophys. Res. Atmos., 123, 491–506, https://doi.org/10.1002/2017JD027431, 2018.

删除[Pan Zhao]: was

删除[Pan Zhao]: New understanding and quantification

删除[Pan Zhao]: the regime dependence of aerosol-cloud interaction for studying aerosol indirect effects,

删除[Pan Zhao]: Lett., 43, 1780–1787

设置格式[Pan Zhao]: 英语(美国)

删除[Pan Zhao]: 2016GL067683, 2016

Chun, J.-Y., Wood, R., Blossey, P., and Doherty, S. J.: Microphysical, macrophysical, and radiative responses of subtropical marine clouds to aerosol injections, Atmos. Chem. Phys., 23, 1345–1368, https://doi.org/10.5194/acp-23-1345-2023, 2023.

Cornwell, G. C., Xiao, H., Berg, L. K., and Burrows, S. M.: Simulated dust transport in the convective boundary layer, J. Geophys. Res. Atmos., 126, e2020JD033429, https://doi.org/10.1029/2020JD033429, 2021.

Dhandapani, C., Kaul, C. M., Pressel, K. G., Blossey, P. N., Wood, R., and Kulkarni, G.: Sensitivities of Large Eddy Simulations of Aerosol Plume Transport and Cloud Response, J. Adv. Model. Earth Syst., 17, e2024MS004546, https://doi.org/10.1029/2024MS004546, 2025.

Diamond, M. S., Director, H. M., Eastman, R., Possner, A., and Wood, R.: Substantial Cloud Brightening From Shipping in Subtropical Low Clouds, AGU Adv., 1, e2019AV000111, https://doi.org/10.1029/2019AV000111, 2020.

Diamond, M. S., Gettelman, A., Lebsock, M. D., McComiskey, A., Russell, L. M., Wood, R., and Feingold, G.: To assess marine cloud brightening's technical feasibility, we need to know what to study—and when to stop, Proc. Natl. Acad. Sci. USA, 119, e2118379119, https://doi.org/10.1073/pnas.2118379119, 2022.

Erfani, E., Wood, R., Blossey, P., Doherty, S. J., and Eastman, R.: Building a comprehensive library of observed Lagrangian trajectories for testing modeled cloud evolution, aerosol-cloud interactions, and marine cloud brightening, Atmos. Chem. Phys., 25, 8743–8768, https://doi.org/10.5194/acp-25-8743-2025, 2025.

Feingold, G., Ghate, V. P., Russell, L. M., Blossey, P., Cantrell, W., Christensen, M. W., Diamond, M. S., Gettelman, A., Glassmeier, F., Gryspeerdt, E., Haywood, J., Hoffmann, F., Kaul, C. M., Lebsock, M., McComiskey, A. C., McCoy, D. T., Ming, Y., Mülmenstädt, J., Possner, A., Prabhakaran, P., Quinn, P. K., Schmidt, K. S., Shaw, R. A., Singer, C. E., Sorooshian, A., Toll, V., Wan, J. S., Wood, R., Yang, F., Zhang, J., and Zheng, X.: Physical science research needed to evaluate the viability and risks of marine cloud brightening, Sci. Adv., 10, eadi8594, https://doi.org/10.1126/sciadv.adi8594, 2024.

Fountoukis, C. and Nenes, A.: Continued development of a cloud droplet formation parameterization for global climate models, J. Geophys. Res. Atmos., 110, D11212, https://doi.org/10.1029/2004JD005591, 2005.

Ghate, V. P., Miller, M. A., Albrecht, B. A., and Fairall, C. W.: Thermodynamic and radiative structure of stratocumulus-topped boundary layers, J. Atmos. Sci., 72, 430-451, https://doi.org/10.1175/JAS-D-13-0313.1, 2015.

Glassmeier, F., Hoffmann, F., Johnson, J. S., Yamaguchi, T., Carslaw, K. S., and Feingold, G.: Aerosol-cloud-climate cooling overestimated by ship-track data, Science, 371, 485–489, https://doi.org/10.1126/science.abd3980, 2021.

Grabowski, W. W. and Wang, L.-P.: Growth of Cloud Droplets in a Turbulent Environment, Annu. Rev. Fluid Mech., 45, 293–324, https://doi.org/10.1146/annurev-fluid-011212-140750, 2013.

Hanna, S. R., Briggs, G. A., and Hosker, R. P.: Handbook on atmospheric diffusion, US Dept. of Energy, Springfield, Va, 102 pp., 1982.

Hernandez-Jaramillo, D. C., Harrison, L., Kelaher, B., Ristovski, Z., and Harrison, D. P.: Evaporative Cooling Does Not Prevent Vertical Dispersion of Effervescent Seawater Aerosol for Brightening Clouds, Environ. Sci. Technol., 57, 20559–20570, https://doi.org/10.1021/acs.est.3c04793, 2023.

删除[Pan Zhao]: Chen

删除[Pan Zhao]: ., Liu,

删除[Pan Zhao]: Zhang, M

删除[Pan Zhao]: Peng, Y.: Height Dependency

删除[Pan Zhao]: Aerosol-Cloud Interaction Regimes, J. Geophys. Res.

删除[Pan Zhao]: ., 123, 491–506

删除[Pan Zhao]: 1002/2017JD027431, 2018

删除[Pan Zhao]: Fast, J. D., Gustafson, W. I., Easter, R

删除[Pan Zhao]: . C., Zaveri, R. A., Barnard, J. C., Chapman, E. G., Grell, G. A., and Peckham, S. E.: Evolution of ozone, particulates, and aerosol direct radiative forcing in the vicinity of Houston using a fully coupled meteorology-chemistry-aerosol model, J. Geophys. Res. Atmos., 111, D22205, https://doi.org/10.1029/2005JD006721, 2006.

设置格式[Pan Zhao]: 英语(美国)

Hernandez-Jaramillo, D. C., Harrison, L., Gunner, G., McGrath, A., Junkermann, W., Lieff, W., Hacker, J., Rosenfeld, D., Kelaher, B., and Harrison, D. P.: First generation outdoor marine cloud brightening trial increases aerosol concentration at cloud base height, Environ. Res. Lett., 20, 054065, https://doi.org/10.1088/1748-9326/adccd7, 2025.

Hersbach, H., Bell, B., Berrisford, P., Hirahara, S., Horányi, A., Muñoz-Sabater, J., Nicolas, J., Peubey, C., Radu, R., Schepers, D., Simmons, A., Soci, C., Abdalla, S., Abellan, X., Balsamo, G., Bechtold, P., Biavati, G., Bidlot, J., Bonavita, M., De Chiara, G., Dahlgren, P., Dee, D., Diamantakis, M., Dragani, R., Flemming, J., Forbes, R., Fuentes, M., Geer, A., Haimberger, L., Healy, S., Hogan, R. J., Hólm, E., Janisková, M., Keeley, S., Laloyaux, P., Lopez, P., Lupu, C., Radnoti, G., De Rosnay, P., Rozum, I., Vamborg, F., Villaume, S., and Thépaut, J.: The ERA5 global reanalysis, Q. J. R. Meteorol. Soc., 146, 1999–2049, https://doi.org/10.1002/qj.3803, 2020.

Hess, M., Koepke, P., and Schult, I.: Optical properties of aerosols and clouds: The software package OPAC, Bull. Am. Meteorol. Soc., 79, 831–844, https://doi.org/10.1175/1520-0477(1998)079<0831:OPOAAC>2.0.CO;2, 1998.

Hoffmann, F. and Feingold, G.: Cloud Microphysical Implications for Marine Cloud Brightening: The Importance of the Seeded Particle Size Distribution, J. Atmos. Sci., 78, 3247–3262, https://doi.org/10.1175/JAS-D-21-0077.1, 2021.

Hoffmann, F., Mayer, B., and Feingold, G.: A parameterization of interstitial aerosol extinction and its application to marine cloud brightening, J. Atmos. Sci., 79, 2849–2862, https://doi.org/10.1175/JAS-D-22-0047.1, 2022.

Iacono, M. J., Delamere, J. S., Mlawer, E. J., Shephard, M. W., Clough, S. A., and Collins, W. D.: Radiative forcing by long-lived greenhouse gases: Calculations with the AER radiative transfer models, J. Geophys. Res. Atmos., 113, D13103, https://doi.org/10.1029/2008JD009944, 2008.

Jaeglé, L., Quinn, P. K., Bates, T. S., Alexander, B., and Lin, J.-T.: Global distribution of sea salt aerosols: new constraints from in situ and remote sensing observations, Atmos. Chem. Phys., 11, 3137–3157, https://doi.org/10.5194/acp-11-3137-2011, 2011.

Janjić, Z. I.: The step-mountain eta coordinate model: Further developments of the convection, viscous sublayer, and turbulence closure schemes, Mon. Weather Rev., 122, 927–945, https://doi.org/10.1175/1520-0493(1994)122<0927:TSMECM>2.0.CO;2, 1994.

Jenkins, A. K. L. and Forster, P. M.: The inclusion of water with the injected aerosol reduces the simulated effectiveness of marine cloud brightening, Atmos. Sci. Lett., 14, 164–169, https://doi.org/10.1002/asl2.434, 2013.

Jenkins, A. K. L., Forster, P. M., and Jackson, L. S.: The effects of timing and rate of marine cloud brightening aerosol injection on albedo changes during the diurnal cycle of marine stratocumulus clouds, Atmos. Chem. Phys., 13, 1659–1673, https://doi.org/10.5194/acp-13-1659-2013, 2013.

Kainz, J., Harrison, D. P., and Hoffmann, F.: Marine cloud brightening of cumulus clouds: from the sprayer to the cloud, Atmos. Chem. Phys., 26, 9443–9451, https://doi.org/10.5194/acp-26-9443-2026, 2026.

Koepke, P., Hess, M., Schult, I., and Shettle, E. P.: Global aerosol data set, MPI Report No. 243, Max Planck Institute for Meteorology, Hamburg, Germany, 44 pp., https://doi.org/10.17617/2.3365749, 1997.

Latham, J.: Control of global warming?, Nature, 347, 339–340, https://doi.org/10.1038/347339b0, 1990.

设置格式[Pan Zhao]: 英语(美国)

设置格式[Pan Zhao]: 英语(美国)

设置格式[Pan Zhao]: 英语(美国)

删除[Pan Zhao]: 1994.

删除[Pan Zhao]: Jia, Y., Tegtmeier, S., Atlas,

删除[Pan Zhao]: E.,

删除[Pan Zhao]: Quack, B.: How

删除[Pan Zhao]: emissions of bromoform impact

删除[Pan Zhao]: remote atmosphere

删除[Pan Zhao]: 19, 11089–11103

删除[Pan Zhao]: 19-11089-2019, 2019

Latham, J., Bower, K., Choularton, T., Coe, H., Connolly, P., Cooper, G., Craft, T., Foster, J., Gadian, A., Galbraith, L., Iacovides, H., Johnston, D., Launder, B., Leslie, B., Meyer, J., Neukermans, A., Ormond, B., Parkes, B., Rasch, P., Rush, J., Salter, S., Stevenson, T., Wang, H., Wang, Q., and Wood, R.: Marine cloud brightening, Philos. Trans. R. Soc. A, 370, 4217–4262, https://doi.org/10.1098/rsta.2012.0086, 2012.

Maalick, Z., Korhonen, H., Kokkola, H., Kühn, T., and Romakkaniemi, S.: Modelling artificial sea salt emission in large eddy simulations, Philos. Trans. R. Soc. A, 372, 20140051, https://doi.org/10.1098/rsta.2014.0051, 2014.

Matheou, G. and Teixeira, J.: Sensitivity to Physical and Numerical Aspects of Large-Eddy Simulation of Stratocumulus, Mon. Weather Rev., 147, 2621–2639, https://doi.org/10.1175/MWR-D-18-0294.1, 2019.

McMichael, L. A., Schmidt, M., Wood, R., Blossey, P. N., and Patel, L.: Exploring ship track spreading rates with a physics-informed Langevin particle parameterization, Geosci. Model Dev., 17, 7867–7885, https://doi.org/10.5194/gmd-17-7867-2024, 2024.

McMichael, L. A., Erfani, E., Wood, R., and von Salzen, K.: Estimating Twomey forcing sensitivity to aerosol plume spreading rates, EGUsphere [preprint], https://doi.org/10.5194/egusphere-2026-2730, 2026.

Mellado, J. P.: Cloud-top entrainment in stratocumulus clouds, Annu. Rev. Fluid Mech., 49, 145-169, https://doi.org/10.1146/annurev-fluid-010816-060231, 2017.

Morales Betancourt, R. and Nenes, A.: Understanding the contributions of aerosol properties and parameterization discrepancies to droplet number variability in a global climate model, Atmos. Chem. Phys., 14, 4809–4826, https://doi.org/10.5194/acp-14-4809-2014, 2014.

Nenes, A., Ghan, S., Abdul-Razzak, H., Chuang, P. Y., and Seinfeld, J. H.: Kinetic limitations on cloud droplet formation and impact on cloud albedo, Tellus B, 53, 133–149, https://doi.org/10.1034/j.1600-0889.2001.d01-12.x, 2001.

O'Dowd, C. D. and de Leeuw, G.: Marine aerosol production: a review of the current knowledge, Philos. Trans. R. Soc. A, 365, 1753–1774, https://doi.org/10.1098/rsta.2007.2043, 2007.

Peng, Y., Lohmann, U., and Leaitch, R.: Importance of vertical velocity variations in the cloud droplet nucleation process of marine stratus clouds, J. Geophys. Res. Atmos., 110, D21202, https://doi.org/10.1029/2004JD004922, 2005.

Prabhakaran, P., Hoffmann, F., and Feingold, G.: Evaluation of Pulse Aerosol Forcing on Marine Stratocumulus Clouds in the Context of Marine Cloud Brightening, J. Atmos. Sci., 80, 1585–1604, https://doi.org/10.1175/JAS-D-22-0207.1, 2023.

Quinn, P. K., Coffman, D. J., Johnson, J. E., Upchurch, L. M., and Bates, T. S.: Small fraction of marine cloud condensation nuclei made up of sea spray aerosol, Nat. Geosci., 10, 674–679, https://doi.org/10.1038/ngeo3003, 2017.

Rasch, P. J., Hirasawa, H., Wu, M., Doherty, S. J., Wood, R., Wang, H., Jones, A., Haywood, J., and Singh, H.: A protocol for model intercomparison of impacts of marine cloud brightening climate intervention, Geosci. Model Dev., 17, 7963–7994, https://doi.org/10.5194/gmd-17-7963-2024, 2024.

Russell, L. M., Seinfeld, J. H., Flagan, R. C., Ferek, R. J., Hegg, D. A., Hobbs, P. V., Wobrock, W., Flossmann, A. I., O'Dowd, C. D., Nielsen, K. E., and Durkee, P. A.: Aerosol dynamics in ship tracks, J. Geophys. Res. Atmos., 104, 31077–31095, https://doi.org/10.1029/1999JD900985, 1999.

设置格式[Pan Zhao]: 英语(美国)

删除[Pan Zhao]: O'Dowd

设置格式[Pan Zhao]: 英语(美国)

删除[Pan Zhao]: O'Dowd

Rutan, D. A., Kato, S., Doelling, D. R., Rose, F. G., Nguyen, L. T., Caldwell, T. E., and Loeb, N. G.: CERES synoptic product: Methodology and validation of surface radiant flux, J. Atmos. Oceanic Technol., 32, 1121 – 1143, https://doi.org/10.1175/JTECH-D-14-00165.1, 2015.

Salter, S., Sortino, G., and Latham, J.: Sea-going hardware for the cloud albedo method of reversing global warming, Philos. Trans. R. Soc. A, 366, 3989–4006, https://doi.org/10.1098/rsta.2008.0136, 2008.

Skamarock, W. C., Klemp, J. B., Dudhia, J., Gill, D. O., Liu, Z., Berner, J., Wang, W., Powers, J. G., Duda, M. G., Barker, D. M., and Huang, X.-Y.: A Description of the Advanced Research WRF Model Version 4, NCAR Tech. Note NCAR/TN-556+STR, 145 pp., https://doi.org/10.5065/1dfh-6p97, 2019.

Stevens, B.: Entrainment in stratocumulus-topped mixed layers, Q. J. R. Meteorol. Soc., 128, 2663–2690, https://doi.org/10.1256/qj.01.202, 2002.

Tewari, M., Chen, F., Wang, W., Dudhia, J., LeMone, M. A., Gayno, G., Wegiel, J., and Cuenca, R. H.: Implementation and verification of the unified NOAH land surface model in the WRF model, 20th Conference on Weather Analysis and Forecasting/16th Conference on Numerical Weather Prediction, Seattle, WA, 11–15 January 2004, 11–15, 2004.

Thompson, G., Field, P. R., Rasmussen, R. M., and Hall, W. D.: Explicit Forecasts of Winter Precipitation Using an Improved Bulk Microphysics Scheme. Part II: Implementation of a New Snow Parameterization, Mon. Weather Rev., 136, 5095–5115, https://doi.org/10.1175/2008MWR2387.1, 2008.

VanReken, T. M., Rissman, T. A., Roberts, G. C., Varutbangkul, V., Jonsson, H. H., Flagan, R. C., and Seinfeld, J. H.: Toward aerosol/cloud condensation nuclei (CCN) closure during CRYSTAL-FACE, J. Geophys. Res. Atmos., 108, 4633, https://doi.org/10.1029/2003JD003582, 2003.

Vogelezang, D. H. P. and Holtslag, A. A. M.: Evaluation and model impacts of alternative boundary-layer height formulations, Bound.-Layer Meteorol., 81, 245-269, https://doi.org/10.1007/BF02430331, 1996.

Wang, H., Rasch, P. J., and Feingold, G.: Manipulating marine stratocumulus cloud amount and albedo: a process-modelling study of aerosol-cloud-precipitation interactions in response to injection of cloud condensation nuclei, Atmos. Chem. Phys., 11, 4237–4249, https://doi.org/10.5194/acp-11-4237-2011, 2011.

Wood, R.: Stratocumulus Clouds, Mon. Weather Rev., 140, 2373–2423, https://doi.org/10.1175/MWR-D-11-00121.1, 2012.

Wood, R.: Assessing the potential efficacy of marine cloud brightening for cooling Earth using a simple heuristic model, Atmos. Chem. Phys., 21, 14507–14533, https://doi.org/10.5194/acp-21-14507-2021, 2021.

Wood, R. and Bretherton, C. S.: Boundary layer depth, entrainment, and decoupling in the cloud-capped subtropical and tropical marine boundary layer, J. Climate, 17, 3576-3588, https://doi.org/10.1175/1520-0442 (2004) 017<3576:BLDEAD> 2.0.CO;2, 2004.

Xue, H., Feingold, G., and Stevens, B.: Aerosol Effects on Clouds, Precipitation, and the Organization of Shallow Cumulus Convection, J. Atmos. Sci., 65, 392–406, https://doi.org/10.1175/2007JAS2428.1, 2008.

Zelinka, M. D., Randall, D. A., Webb, M. J., and Klein, S. A.: Clearing clouds of uncertainty, Nat. Clim. Change, 7, 674–678, https://doi.org/10.1038/nclimate3402, 2017.

删除[Pan Zhao]: Stohl, A., Forster, C., Frank, A., Seibert, P., and Wotawa, G.: Technical note: The Lagrangian particle dispersion model FLEXPART version 6.2, Atmos. Chem. Phys., 5, 2461–2474, https://doi.org/10.5194/acp-5-2461-2005, 2005.

设置格式[Pan Zhao]: 英语(美国)